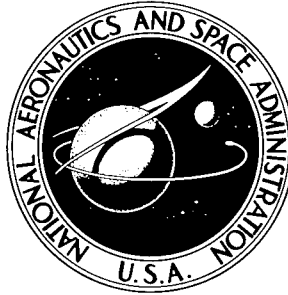PA
12,051R

NASA TECHNICAL NOTE

NASA TN D-2472

HYPERVELOCITY IMPACT DAMAGE CHARACTERISTICS IN ARMORED SPACE RADIATOR TUBES

by Seymour Lieblein, Nestor Clough

Lewis Research Center
Cleveland, Ohio

and A. R. McMillan

General Motors Corporation
Defense Research Laboratories
Santa Barbara, Calif.

19960624 009

DISCLAIMER NOTICE

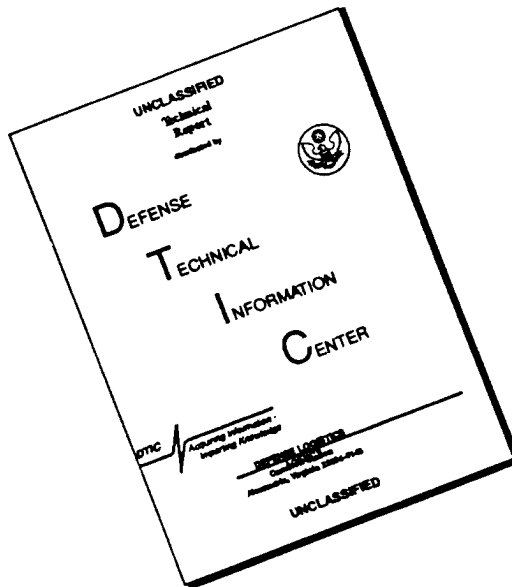THIS DOCUMENT IS BEST QUALITY AVAILABLE. THE COPY FURNISHED TO DTIC CONTAINED A SIGNIFICANT NUMBER OF PAGES WHICH DO NOT REPRODUCE LEGIBLY.

HYPERVELOCITY IMPACT DAMAGE CHARACTERISTICS IN

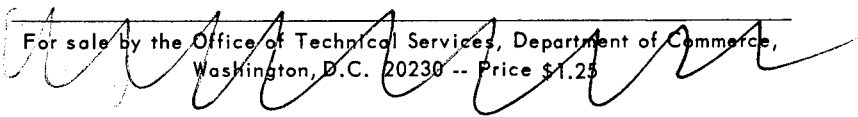# ARMORED SPACE RADIATOR TUBES

By Seymour Lieblein, Nestor Clough

Lewis Research Center
Cleveland, Ohio

and A. R. McMillan

General Motors Corporation
Defense Research Laboratories
Santa Barbara, Calif.

NATIONAL AERONAUTICS AND SPACE ADMINISTRATION

HYPERVELOCITY IMPACT DAMAGE CHARACTERISTICS IN ARMORED SPACE RADIATOR TUBES

by Seymour Lieblein, Nestor Clough,

Lewis Research Center

and

A. R. McMillan

General Motors Corporation
Defense Research Laboratories
Santa Barbara, California

SUMMARY

Described herein are the results of an exploratory experimental research program to determine the damage that might be inflicted on space radiator configurations by the impact of a meteoroid. The meteoroid hazard is discussed, and the present knowledge of crater formation under conditions of hypervelocity impact is analyzed The experimental program was conducted under NASA contract on the ballistics range facilities of the General Motors Corporation Defense Research Laboratories in Santa Barbara, California. Glass projectiles of approximately 0.016 and 0.040 gram were accelerated to velocities of 23,000 to 26,000 feet per second and impacted against unfilled radiator tube configurations in vacuum. Variables such as tube liner thickness, tube inner diameter, armor thickness, operating temperature, and angle of impact were considered for aluminum and columbium alloy targets.

Significant differences between hypervelocity impact into flat plates and into aluminum and columbium tubes were observed. The limited results indicated that internal surface dimpling and spalling, as well as perforation, may be important considerations in radiator tube design.

INTRODUCTION

An analytical approach to the definition and composition of meteoroids and the assessment of the meteoroid damage problem for waste-heat radiators of space power systems are presented in reference 1. The analysis of reference 1 represents a detailed application of the current concepts of the nature of meteoroid behavior and their impact effects. Specific insight into the general damage likely to be incurred by a meteoroid collision can be obtained, for example, from references 2 to 4. Unfortunately, however, very little background exists in the area of the phenomena of hypervelocity meteoroid impact under conditions likely to be experienced by a space radiator. In particular, it is necessary to compare the predicted meteoroid hazard for the specified mission of the vehicle against an evaluation of the meteoroid protection associated with the radiator structure as determined by the radiator material, the radiator construction and configuration, the inflight operational environment of high material temperatures and low ambient pressures, and the reaction of a pressurized liquid or gas in the tube.

An experimental research program was undertaken to assess the impact damage by a meteoroid against a variety of targets simulating radiator materials and configurations under operating conditions of elevated temperature and low ambient pressure. The research was directed toward defining significant damage phenomena and obtaining data related to the broad concepts of protecting radiators against damage from impacting meteoroids. The experimental program was conducted on the ballistics range facilities of the General Motors Corporation Defense Research Laboratories, Santa Barbara, California (NASA Contract No. NASw-468).

The program was intended to explore the nature of hypervelocity impact damage in radiator tube configurations typical of application to space power systems such as SNAP-8. Preliminary results of this study have been obtained with aluminum and columbium - 1-percent-zirconium tube configurations as reported in reference 5.

The complete results of this program, including photographs of the impacted targets and the complete data listing, are reported herein, following a brief review of the meteoroid hazard.

DESCRIPTION OF HAZARD

The immediate concerns to the designer of a space radiator system are the likelihood of collision with meteoroids of given properties in space and the resultant damage. Since it is impossible to control the occurrence of meteoroids in space, the designer must provide shielding that is capable of protecting a radiator from impact damage by the largest meteoroid it is expected to encounter for a specified survival probability, flight path, and exposure time. Consequently, the meteoroid hazard to a space vehicle must be considered in terms of frequency of encounter, direction of influx, mass distribution, relative velocity, physical properties of meteoroids, vulnerable area of the radiator, and mission time. Because of the large surface areas involved, meteoroids of most vital interest to radiator designers are the particulate matter in the range of mass from 10^{-2} to 10^{-4} gram, large enough and frequent enough to be of some hazard. Also of concern is the finer material capable of etching the high emittance coating of the radiator surface. The techniques used in the recent publications by Whipple (ref. 6) and by Dubin and McCracken (ref. 7), in which the frequency of occurrence of meteoroids in space has been predicted, include photographic and radar measurements as well as rocket and satellite measurements. From an analysis of these data it is possible to assess the meteoroid hazard to space radiators in terms of the meteoroid properties, the vulnerable area of typical radiator systems, the mission time, and the anisotropic meteoeroid flux expected for a given vehicle voyage (ref. 1).

If it is assumed that the frequency of occurrence of meteoroids can be predicted, it is now necessary to define the impact damage likely to be sustained by a given radiator design. For space power systems involving liquid metal fluids, the radiator may appear as in figure 1. The fluid-carrying tubes will most likely be composed of a thin corrosion-resisting inner liner sur-

rounded by a sleeve of impact-resisting armor. A typical radiator finned-tube segment is shown in figure 2. The finned radiator segment is made of cast aluminum alloy armor (0.400 in. thick) over a Haynes Stellite Alloy 25 (HS-25) tube liner (0.020 in. thick). The crater shown in figure 2 was caused by a 1/8-inch-diameter glass sphere (0.038 g) impacting at 23,000 feet per second. The kinetic energy of the impacting pellet is characteristic of meteoroid energies likely to be encountered in space. Although the crater depth of 0.3 inch did not result in perforation of the tube, the intense shock produced beneath the crater caused a dimpling of the liner and consequent constriction of the fluid passage of the tube. This particular shot was fired at room temperature. Hence, the aluminum armor behaved in a semibrittle fashion evidenced by a brittle spalling around the periphery of the crater.

A physical description of the mechanism of crater formation in simple plate targets under normal hypervelocity impact is now possible within the state of the art. Many experimental data are available, and empirical relations have been established to describe the phenomena. Various models that have evolved from the combined theoretical and experimental studies by many researchers have been illustrated schematically in references 4 and 8.

Although there exists no detailed mathematical theory by which to describe the phenomena of normal hypervelocity impact, relations have been established and verified experimentally. Some of these relations will be discussed, and their ability to predict accurately the resultant crater dimensions will be noted. The most important of the phenomena observed in previous studies is that a linear relation exists between the volume of the crater resulting from hypervelocity impact and the energy of the impacting projectile. The importance of target resistance to shear deformation at high-strain rates is seen to be a controlling parameter to the final crater volume. For example, the Brinell hardness number was found to provide a surprisingly good criterion for assigning a value to the strength of the target. Other significant strength parameter correlations may be determined, however.

Since space radiators may be operating at temperatures from around 500° to 2000° F, the effects of raising the target temperature will be evidenced by an increase in the resultant damage, as reported in reference 4. Therefore, it is necessary to test space radiator tubes under simulated operating conditions in order that a proper appraisal may be made of the damage that has been effected.

EXPERIMENTAL PROGRAM

The overall objectives of the NASA radiator protection program are three-fold: first, to define the principal damage mechanisms involved in the hypervelocity impact of particles against radiator tubes; second, to evaluate the relative effectiveness of various protection methods and concepts; and third, to conduct a systematic study of the significant parameters involved so that a large body of realistic design data covering a wide range of applications can be obtained. In most cases the experimental work will deal with realistic tube

targets of applicable materials and configurations at temperatures and in environments characteristic of the radiator design operation.

In general, two basic protection concepts are currently being considered in radiator design (ref. 1). The first, and simplest, is the solid armor approach in which a mass of material is used to surround the fluid carrying members. In this case the design problem is to allow for just enough mass (i.e., thickness) that will prevent a predefined damage to the configuration. In the second approach, called the bumper approach, various displaced shield configurations are utilized to break up the projectile into smaller particles allowing the use of less primary armor material. Examples of radiator geometries embodying the armor and bumper approaches are given in figure 3. The bumper concepts, for effective evaluation, however, must also include consideration of the effects of heat-transfer impedence.

In the effort contained in the present program, initial work has been directed toward an experimental study of the armor protection approach. The armor approach was undertaken first because it was felt that the large amount of supporting data available from flat plate firings would enhance an early generation of usable design data. An exploratory set of firings into armored tubes was therefore set up to investigate tube damage phenomena (cratering and internal spalling) and to indicate some of the variables involved. It was also hoped to obtain a general grasp of real tube effects to aid in the direction and detailing of the subsequent effort. In addition, targets and conditions were prescribed for this first phase that were characteristic of current radiator system designs (such as SNAP-8) so that any significant results attained could find immediate application.

For armored tubes the principal variables expected to influence damage are armor material and thickness, temperature, inner (corrosion resisting) liner material and thickness, angle of impact, and internal fluid (liquid or gas). The first phase of the program was therefore set up to include most of these variables. Tube configurations used were solid 356-T51 cast aluminum tubes on a HS-25 inner liner, and solid columbium - 1-percent-zirconium alloy tubes. The specific shots called for in this first phase are outlined in table I. It was intended to conduct these firings with 3/32-inch-diameter glass projectiles at a nominally constant velocity. Equivalent protection thicknesses for the aluminum and columbium tubes were determined according to the impact relations of reference 1.

EXPERIMENTAL TECHNIQUES

Range and Monitoring Instrumentation

All of the tests to date were conducted on a ballistics range, which is fully described in reference 9. The basic equipment consists of a light-gas gun, a 20-foot free-flight range, and an impact chamber. The 0.22-inch caliber accelerated-reservoir light-gas gun is shown in figure 4. With this gun it was possible to launch cylindrical plastic models to velocities of 32,000 feet per second or saboted metal or glass spheres to velocities of 28,000 feet per second.

The accelerated-reservoir light-gas gun consists of a combustion chamber in which a smokeless powder is used to accelerate a polyethylene pump piston down an 18-foot-long, 1-inch-inside-diameter pump tube. In so doing, the pistons compress hydrogen as the driver gas to a nominal pressure of 20,000 to 30,000 pounds per square inch. At this pressure a break valve opens at the front end of the high-pressure coupling and thus releases the hydrogen gas into the launch tube behind the model. As the model begins to travel in the 4-foot-long launch tube, the pump piston enters the tapered section of the high-pressure coupling. The front face of the pump piston is accelerated and thus a constant base pressure is maintained behind the model during launch. The projectile is launched into the flight range and travels 20 feet before impacting the target. Prior to impact, the projectile travels through a surge chamber (in which the model is separated from the sabot) and then into the velocity chamber. Here the position and time of flight of the projectile are recorded at each of three spark shadowgraph stations (the octagonal chamber shown in fig. 5). When the model interrupts a photo beam, electronic counters are started, a short duration spark is set off at each station, and a film plate is exposed. The measurements of time and distance between stations serve to determine the velocity of the projectile along its trajectory and, in particular, at the target. The accuracy of the impact velocity determined in this manner is better than ±1 percent.

The flight of the model is terminated in a specially constructed impact chamber (fig. 5) that has six viewing ports. Two large windows are located on opposite sides of the target area, and four smaller windows are located on the front of the chamber. A full-size door acts as the rear wall of the chamber to allow easy insertion and removal of the targets. The targets are held by a mount that is supported by two rails on the floor of the chamber. This design allows placement of the target at a uniform longitudinal position with respect to the viewing ports. A variety of targets can be accommodated.

Since the investigation of the damage to a radiator target requires that the targets be impacted while under a simulated space environment, it was necessary to conduct the tests with the target at an elevated temperature while in a simulated space environment of low ambient pressure. A typical target holder with the heater elements is shown in figure 6. This target holder permits mounting the radiator segments and heating them to temperatures up to 1000° F. The requirement for low ambient pressures was met by sealing the impact and velocity chambers and by pumping down to pressures of less than 1 millimeter of mercury. Air, or any number of desired gas mixtures, can be introduced into the chambers as a test medium. In order to prevent oxidation of the heated targets in these tests, helium was used as the test gas. A vacuum gage, calibrated for helium gas, provided accurate pressure measurements within the chambers.

Photographic equipment was used to monitor the impact phenomena. A camera capable of framing rates as high as 1.4 million frames per second was used to record precisely the incoming projectile velocity, the phenomena of impact flash, and the motion, velocity, and, in a rough sense, the quantity of minute particles being ejected from the crater. With this camera it was also possible to observe, in a plane across the surface of the target, the growth of the crater in time. A typical film sequence of a 1/8-inch glass sphere impacting

the space radiator segment of figure 2 at 23,000 feet per second is shown in figure 7.

The ballistics range is also equipped with four channels of flash radiographic equipment capable of viewing the impact at any four preselected times during the crater formation (fig. 5). Each X-ray pulse is 0.07 microsecond in duration at a peak output of 100 kilovolts at 1400 amperes. Flash X-ray instrumentation is particularly useful to "see" through the ejecta debris from the crater to determine the composition of the debris, that is, vapor or solid particles. The combination of X-ray and camera optical records provides a detailed pictorial record of the process of crater formation.

Target Preparation

The assessment of target damage to the space radiator is complex and requires precise definition. Prior to testing any of the targets, each target was classified according to material properties (as indicated by the manufacturer's specification) and condition of the material (as indicated by visual examination). Since the tests were intended to simulate actual operating conditions, each target was annealed for 8 hours at the test temperature before the shot was fired. In the tests conducted thus far, the annealing and test temperatures were 700° F. This pretreatment procedure was significant in that the aluminum targets underwent a phase change at 700° F after several hours of annealing, which resulted in reducing the Brinell hardness number from a nominal 52 to a value of 36. The Brinell hardness number is used here as a measure of the strength of the material; hence, the lower the number, the more damage expected on impact (ref. 4). Following the shot, the targets were cooled to room temperature and the damage assessed.

EXPERIMENTAL RESULTS

A complete tabulation of the results and identifying parameters for all data shots fired in conjunction with this phase of the program is given in table II. Crater depth and dimple height were defined with respect to the original surfaces as shown in figure 8.

In addition to measurements of crater depth and diameter, targets were sectioned to show the extent and nature of the damage. To assist in reporting the observed damage, a damage evaluation code was established as shown in figure 9. The firings reported in table II include most of the specific shots called for in table I and additional exploratory or development shots into the subject targets that supplied useful information. In many cases it was not possible to achieve the exact conditions specified. The velocities achieved were in the range from 23,000 to 26,000 feet per second. The projectiles used had a nominal density of 2.7 grams per cubic centimeter.

The analysis of the experiments will be described under two major headings. The first, Qualitative Analysis, will include qualitative observations and comparisons. Quantitative assessment of crater depth and onset of spalling will be made in the section Quantitative Analysis.

6

Qualitative Analysis

Mass scaling. - Meteoroid mass scaling effects are considered by comparing the damage caused by the impact of two projectiles, one a 3/32-inch glass sphere and the second a 1/8-inch glass sphere. Each sphere impacted an aluminum-armored HS-25 tube at a velocity around 23,250 feet per second (fig. 10). The targets were at an average environmental operating temperature of 715° F. These projectiles, weighing 0.0163 and 0.0413 gram, respectively, fall into the meteoroid mass-frequency distribution area of interest for radiators (ref. 1).

As shown in figure 10, the 3/32-inch glass sphere did not perforate the armor but did cause a dimpling of the inner liner. The 1/8-inch glass sphere, on the other hand, produced a larger crater diameter and complete perforation of the aluminum armor and the HS-25 liner. Hence, under these conditions of target temperature and projectile density, the "ballistic limit" of this configuration can be defined as being between a meteoroid kinetic energy of 302 to 762 foot-pounds.

Target temperature. - Although it was shown in reference 4 that by increasing the target temperature one could achieve greater damage to a simple metal plate target, it was not known how the increased temperature would affect a composite tube target such as those selected for these tests. In one test, a 1/8-inch glass sphere was fired at an average velocity of 23,300 feet per second into each of two targets, one at room temperature and the other at 700° F (fig. 11). In both cases the radiator complex was perforated. In the case of the target at 700° F, however, the crater area was greater than for the target at room temperature. In addition, the target at room temperature exhibited evidence of brittle spalling around the periphery of the crater, which is indicative of the greater hardness or lower ductility of the material.

Aluminum targets impacted by a 3/32-inch glass sphere at 400° and 700° F are shown in figure 12(a). The increase in temperature resulted in an increase in both crater depth and diameter, but it did not affect the height of the dimple in the liner. Sections of these targets taken at the center of the crater and a saw-cut away are shown in figure 12(b); the armor material did not follow into the void created by the dimpled liner away from the point of maximum crater depth.

Impact angle. - The next variable known to affect seriously the damage sustained by a target under hypervelocity impact is that of the impact angle of the projectile to the surface of the target. Figure 13 shows the results of a 3/32-inch glass sphere impacting aluminum armor targets at 27° and 70° from the normal at around 25,000 feet per second at room temperature (photographs were taken normal to the resultant crater). Oblique impacts at two angles for aluminum armor targets at 700° F are shown in figure 14. Several important results should be pointed out. First, all the craters appear hemispherical, thus assuring that the impacts were typical of the hypervelocity impact regime. This observation is essentially confirmed by the section photograph of figure 15 (sections taken at maximum crater depth and a saw-cut away). Second, penetration depths and the resulting crater volumes decrease as the impact angle increases. According to previous investigations with plate targets

(refs. 4 and 10), these effects can be accounted for empirically by measuring the energy of the attacking projectile in terms of its normal component of velocity. Hence, as the angle of obliquity is increased, the energy of the projectile and the corresponding penetration depth should diminish with the square of the cosine of the angle of impact.

The phenomena of reduced penetration with angle of obliquity was also observed for the columbium - 1-percent-zirconium tube targets (fig. 16). The results of figure 16 add further verification to the observation that, providing the normal component of velocity of the projectile exceeds that required for hypervelocity cratering, the resultant crater will be a hemisphere, although much reduced in volume.

Internal damage. - It was indicated earlier that radiator tube design should also be concerned with the possibility of internal damage effects such as spalling and dimpling even in the absence of a perforation of the tube wall. The existence of such effects in columbium and aluminum tubes was verified as indicated in figure 17. Deleterious effects resulting from the injection of spalled fragments into the flow, from the constriction of the fluid flow, or from the generation of a pressure pulse in a flowing liquid will have to be considered. It is not sufficient, therefore, merely to observe the crater and measure depth of penetration in assessing target impact damage for application to radiator tube configurations.

Inner liner. - The beneficial effects provided by an inner liner can be seen in figure 18. In this figure one target was lined with a 0.020-inch-thick HS-25 liner, while the second target had no liner; the aluminum armor was made thicker, and thus the weight was kept constant. The inner HS-25 liner, although dimpled on the inside, prevented metal spalling into the tube. A section photograph of the target with no liner, target 38, is shown in figure 19. Even when the projectile size was increased to a 1/8-inch sphere, spalling was still prevented by the liner as shown by the target on the right in figure 17, although the dimpling was severe. It can be concluded, therefore, that a tough inner liner is of great importance in preventing spalls from being ejected into the coolant-carrying fluid.

A typical impact crater section of an aluminum target with an HS-25 liner is shown in figure 20. Here the spalling of the armor material beneath the crater itself can be clearly seen, in addition to the dimpled HS-25 liner and the delaminating that has occurred between the liner and the armor. The manner in which the HS-25 liner restricts the flaking and breaking away of the spalled particles is clearly depicted. Of a much more subtle nature is the delaminating that has occurred at a distance far removed from the dimpled section itself. A closeup view of points A and B in figure 20 can be seen in figure 21. Here at magnifications of 120 and 300, respectively, the crater section at points A and B can be seen in detail. At point A severe delaminating has occurred because the HS-25 liner was pulled away from the armor and the bonding material failed. Section B shows another interesting observation. Here it is believed that some delamination is not associated with the formation of the crater, but rather a failure of the bond during the heating of the radiator section prior to impact. The larger coefficient of expansion in aluminum, compared with HS-25, no doubt resulted in a failure of the bond

during the heating process. Delamination can affect radiator performance by reducing section strength and heat-transfer properties.

Tube effect. - In applications of cratering data to radiator tube design, it has been assumed that the depth of penetration in flat plate targets is representative of the penetration into tube walls of identical thickness. This was not found to be the case, however, for a significant effect of tube size on impact damage was observed. Figure 22 shows impact into a columbium - 1-percent-zirconium flat plate (radius = ∞) and into a 0.46-inch inside-diameter columbium - 1-percent-zirconium tube of the same wall thickness under identical test conditions. Complete suppression of spalling was found in the case of the tube, although the depths of penetration were essentially the same. A similar result was obtained for an unlined aluminum tube, as shown in figure 23. The results show the tubular section not perforated, yet the flat plate was completely perforated. A more dramatic example of the tube radius effect with the cast aluminum is shown in figure 24. The section photographs show the results of impact into tubes of 2.5- and 0.125-inch inner diameters under identical conditions and wall thicknesses. Additional photographs of these two targets are shown in figures 25 to 27.

The ability of the tubular target shape to sustain less impact damage is believed to stem from the combined effects of size and inner and outer curvature. If this observed tube size effect is verified by further data, it would indicate a considerable advantage in using small-diameter tubes. The use of such tubes results in a smaller required protection thickness and a smaller perimeter, both of which combine to produce a reduced weight.

Protection criterion. - The final qualitative comparison to be drawn from the experiments conducted is the effect of damage protection criterion. Figure 28 shows an impacted columbium tube and a tube of aluminum armor and HS-25 liner designed for approximately equal weight of protective thickness. The poorer performance of the columbium alloy on this basis is indicated. Figure 29 shows the results of impact into columbium and aluminum-lined tubes designed for equal protection in which the tube wall thicknesses were adjusted to 1.5 P_∞ according to the relation of reference 1. (It should be noted that, in designing a tube to prevent perforation, 1.5 P_∞ is not necessarily a correct value to use. Later studies indicates 1.78 P_∞ is necessary to prevent perforation in 2024-T3 aluminum flat plates (ref. 11).) As shown in the subsequent section entitled "Materials constant," the results of impacts indicate that penetration in the columbium targets was substantially less than expected from analysis.

Quantitative Analysis

The preceding section presented a discussion of some of the principal qualitative observations obtained from the results of the initial firings. In addition to exploring and defining the phenomenological aspects of impact into radiator tube configurations such as the damage mechanisms and principal variables involved, the program also has as its ultimate objective the generation of accurate analytical relations for use in design. Although the initial phase of the program was not specifically designed as a systematic parametric study,

it was possible to obtain some preliminary quantitative information from the firings.

It was pointed out earlier that a detailed mathematical formulation by which to predict accurately the damage done by a meteoroid to space radiator configurations does not exist. The theoretical approaches of Bjork, Riney, Chou, and others[1] have made significant advances in the analytical approach. The treatments, however, do not account in detail for the effects of increased target temperature, variations in target and projectile material, impacts at angles of obliquity, and the spalling, dimpling, or delaminating of thin and composite targets. A number of empirical relations have been offered in the literature (refs. 1, 4, and 12 that do permit at least an approximation of the depth of penetration that might occur under limited conditions. These relations are of the form (ref. 4)

$$P_\infty = K \left(\frac{E}{B_t} \cos^2 \lambda \right)^{1/3} \quad \text{(cgs units)} \tag{1}$$

where $K = 1.82 \times 10^{-3}$ cm/erg$^{1/3}$, or (refs. 1 and 13)

$$P_\infty = \gamma \left(\frac{\rho_p}{\rho_t} \right)^{\varphi} \left(\frac{V \cos \lambda}{C_t} \right)^{2/3} d_p \tag{2}$$

(All symbols are defined in the appendix.) These relations, however, were obtained from impact into thick flat-plate targets, and it is not known to what extent they will be valid for tubular targets.

Some preliminary correlations pertaining to several factors involved in the previous relations for depth of penetration have been established from the initial limited firings. These relate to the effects of target temperature, angle of impact, target material, tube size, and liner thickness. In these plots the values of depth of penetration are the values corrected to a common velocity of 25,000 feet per second according to the two-thirds power of the velocity (designated by P^*). In addition, only penetration values for P/t_a less than 0.75 were included in order to eliminate "thin-target" effects. Each data point is identified by its corresponding target number.

Angle of impact. - The available data on variation of depth of penetration with angle of impact are shown in figure 30 for cast aluminum tubes at two temperatures. The best-fit variations for the $(\cos \lambda)^{2/3}$ relation of equations (1) and (2) are also shown in the figure. On the basis of these analytical relations it was possible to normalize the data with respect to penetration into an infinite target at 25,000 feet per second (P_∞^*), at normal impact

---

[1]For additional papers on hypervelocity impact phenomena see: Proceedings of the Third Symposium on Hypervelocity Impact, Armor Research Foundation, October 1958, the Fourth Symposium on Hypervelocity Impact held at Eglin Air Force Base, Florida, April 1960, and the Fifth Symposium on Hypervelocity Impact held at the Colorado School of Mines, Denver, Colorado, October 1961.

10

$(\lambda = 0)$, as shown in figure 31. It is thus seen that the data are well represented by the $(\cos \lambda)^{2/3}$ relation, which verifies the significance of the normal component of velocity in determining penetration depth for the aluminum tubes.

Target temperature. - The available information on variation of depth of penetration with temperature for normal impact for identical conditions is shown for cast aluminum targets in figure 32. The value of P^* for normal impact was obtained by correcting for angle of impact according to the $(\cos \lambda)^{2/3}$ relation as indicated in figure 31. According to equation (1) the depth of penetration should vary as $(1/B_t)^{1/3}$, and according to equation (2) the variation should follow $(1/Y_t)^{1/3}$. The best fit of the experimental data for the functional variation based on modulus of elasticity and Brinell hardness is shown in figure 31. Values of modulus were obtained from an unpublished NASA compilation of mechanical properties of materials. The data variation is seen to be reasonably described by the analytical relations.

Tube size. - Examination of the data indicated the existence of a tube size effect on depth of penetration. This effect is shown in figure 33 where the depth of penetration for normal impact against ratio of tube wall thickness to outer radius is plotted for aluminum and columbium tubes at 700° F. The lower limiting value of $t_a/R_o = 0$ corresponds to a flat plate, while $t_a/R_o = 1$ represents the upper limit of a solid cylinder. It should be noted that the region of fall off in penetration depth at high values of t_a/R_o corresponds to practical values of tube inner diameter (0.50 in. and less). Although no inner surface damage was observed for these high t_a/R_o points, it is not known whether a quantitatively comparable decrease in required thickness will be observed for the avoidance of incipient spalling or dimpling. It is clear from the photographs of figures 22 to 28, however, that a substantial decrease in spalling and dimpling can be expected for reduced tube size.

The extension of the faired curves through the data points to $t_a/R_o = 0$ permits the normalizing of the data with respect to flat-plate penetration (P^* at $t_a/R_o = 0$) as shown in figure 34. The aluminum and columbium tubes are seen to fall on essentially the same curve, which indicates a possible uniform effect for both materials. The establishment of a general empirical correction relation for tube size on these limited data, however, is considered premature.

Although a good preliminary correlation has been obtained on the basis of the ratio of wall thickness to outer radius, this may not be the most significant physical parameter. It can be reasoned that the size of the tube, the size of the impacting particle, and the ratio of particle diameter to outer radius may also be involved.

Tube liner thickness. - The effects of variation of tube liner thickness on depth of penetration and inner surface dimple height are shown in figure 35 for aluminum armor - HS-25 liner combinations of constant total weight. (Armor thickness decreases with increasing liner thickness.) Depth of penetration is seen to increase with increasing liner thickness. The reason for this is not clear. Since the thick liner shots represent values of P/t_a greater than

11

0.75, the increased penetration may be a "thin-target" effect, or the effect may be due to the interaction of the liner on the shock variations in the armor. It is also observed that depths of penetration greater than the armor thickness can be obtained because of the dimpling of the liner.

Dimpling of the liner is seen to increase as liner thickness decreases, and for some small value of liner thickness the dimple bursts and spalling occurs. (The unlined tube showed considerable spalling.) As long as the liner is sufficiently thick to prevent rupture, it appears that there is a sizable variation in liner thickness that can be used at fixed total weight without risk of puncture, at least for the limits covered in the tests.

Materials constant. - The estimation of depth of penetration using the form of equation (2) involves a material constant that has been reported to vary from around 1.5 to 2.5 (ref. 13). In reference 1, γ is taken as 2.0, and in reference 12, γ is 2.28. The data obtained in the initial phase of the program can also be utilized to obtain an indication of the applicability of these constants. For a tube, equation (2) can be written

$$ \gamma = \frac{\dfrac{P}{d_p}}{\left(\dfrac{\rho_p}{\rho_t}\right)^{\varphi}\left(\dfrac{V\cos\lambda}{C_t}\right)^{2/3}\left(\dfrac{P}{P_\infty}\right)} \tag{3} $$

where P/d_p is based on the measured depth of penetration in the tube target, P/P_∞ is the correction for tube size established in figure 31, and the other values in the denominator are computed from material properties and test conditions (ref. 1, $\varphi = 1/2$; ref. 12, $\varphi = 2/3$).

Values of γ were computed for the applicable data points as indicated in table III for aluminum and columbium - 1-percent-zirconium targets. For the 16 cast aluminum targets, the average value of γ was 2.27, in close agreement with the constant of reference 12. The density of aluminum and that of glass were assumed equal, negating the influence of the difference in φ in references 1 and 12. For the columbium - 1-percent-zirconium targets, however, the calculated average values were substantially lower than the equation values for both references. For the equation of reference 1 ($\varphi = 1/2$), the calculated γ is 1.49; while for the equation of reference 12 ($\varphi = 2/3$), γ is 1.79. The difference between the values for the cast aluminum and the columbium - 1-percent-zirconium alloy targets suggests that the constant γ cannot be taken as a single value for a variety of target materials. Since only four data points are available for the columbium targets, however, and since these targets were heated in air for 8 hours at 700° F prior to impact and therefore became oxidized, further firings into columbium will be necessary to establish firmly the existence of the differences in γ.

The foregoing results, if substantiated, indicate a relatively smaller depth of penetration in columbium than previously estimated. This does not necessarily mean, however, that the armor thickness (and consequently the weight) required to avoid critical damage (spalling or dimpling) will likewise

12

be less. Further tests will be required to establish whether such is indeed the case.

SUMMARY OF RESULTS

An exploratory experimental investigation of hypervelocity impact by glass spheres at around 25,000 feet per second into columbium - 1-percent-zirconium alloy radiator tube targets and cast aluminum targets with and without HS-25 inner liners was conducted to explore effects of target temperature, angle of impact, liner thickness, tube size, and target material. The major findings of the investigation are as follows:

(1) Hypervelocity impact can create spalling and dimpling of the tube inner surface in thicknesses substantially greater than that required to prevent perforation. Spalling and dimpling should therefore be important considerations in tube armor design.

(2) Significant differences between impact into tubes and plates were observed. In general, decreasing the tube size below an outside diameter of about $1\frac{1}{2}$ inch tended to reduce depth of penetration and spalling. An advantage is indicated in using small diameter tubes.

(3) The presence of a thin HS-25 liner on the inside of the cast aluminum armor tended to suppress spalling and permit a greater depth of penetration without puncture. Considerable dimpling can occur, however.

(4) Variation of depth of penetration appeared to correlate well with the normal component of the impact velocity.

(5) Increasing depth of penetration with increasing target temperature up to 700° F appeared to correlate well with the variation of the modulus of elasticity or the Brinell hardness in the target.

(6) The depth of penetration in aluminum was in essential agreement with the predictions of two commonly used empirical relations. The depth of penetration in columbium - 1-percent-zirconium, however, appeared to be substantially lower than predicted by these relations.

Lewis Research Center
    National Aeronautics and Space Administration
        Cleveland, Ohio, May 25, 1964

APPENDIX - SYMBOLS

B_t Brinell hardness number of target

C_t velocity of sound in target, $\sqrt{Y_t g/\rho_t}$

d_p diameter of projectile

E kinetic energy of projectile, ergs

g acceleration of gravity

h dimple height

K constant, 1.82×10^{-3} cm/erg$^{1/3}$, eq. (1)

P depth of penetration in tube target

P_∞ depth of penetration in thick target

P^* depth of penetration in tube target corrected to 25,000 ft/sec

R_o tube outside radius

T temperature

t_a armor thickness

t_l liner thickness

V projectile velocity

Y_t target modulus of elasticity

γ materials constant in penetration equation

φ exponent for density ratio in penetration equation

λ angle of impact (measured from normal)

ρ_p projectile density

ρ_t target density

14

REFERENCES

1. Loeffler, I. J., Lieblein, Seymour, and Clough, Nestor: Meteoroid Protec-
   tion for Space Radiators. Paper 2543-62, ARS, 1962.

2. Bjork, R. L.: Meteoroids vs. Space Vehicles. ARS Jour., vol. 31, no. 6,
   June 1961, pp. 803-807.

3. Jaffe, Leonard D., and Rittenhouse, John B.: Behavior of Materials in
   Space Environments. ARS Jour., vol. 32, no. 3, Mar. 1962, pp. 320-346.

4. Eichelberger, R. J., and Gehring, J. W.: Effects of Meteoroid Impacts on
   Space Vehicles. ARS Jour., vol. 32, no. 10, Oct. 1962, pp. 1583-1591.

5. Gehring, J. W., and Lieblein, S.: Preliminary Results on Effects of Hyper-
   velocity Impact on Space Radiator Tubes. Vol. 11 - Power Systems for
   Space Flight. Prog. in Astronautics, Academic Press, 1963.

6. Whipple, Fred L.: Dust and Meteorites. Astronautics, vol. 7, no. 8,
   Aug. 1962, pp. 40-42.

7. Dubin, M., and McCracken, C. W.: Measurements of Distribution of Inter-
   platetary Dust. Astronomical Jour., vol. 67, no. 5, June 1962,
   pp. 248-256.

8. Maiden, C. J.: Meteoroid Impact. TM 63-203, Defense Res. Labs., General
   Motors Corp., 1963.

9. Anon.: Research Facilities of the Aerospace Operations Department.
   ER 62-201A, Defense Res. Labs., General Motors Corp., 1962.

10. Bryan, G. M.: Oblique Impact of High Velocity Steel Pellets on Lead Tar-
    gets. Proc. of Fifth Symposium on Hypervelocity Impact, vol. 1, pt. 2,
    Apr. 1962, pp. 511-534.

11. McMillan, A. R.: An Investigation of the Penetration of Hypervelocity
    Projectiles into Composite Laminates. Proc. of Sixth Hypervelocity Im-
    pact Symposium, Cleveland (Ohio), Apr. 30 - May 1-2, 1963.

12. Charters, A., and Summers, J. L.: High Speed Impact of Metal Projectiles
    in Targets of Various Materials. Proc. of Third Hypervelocity Impact
    Symposium, Armor Res. Foundation, Chicago (Ill.) Oct. 1958.

13. Rodriquez, David: Meteoroid Shielding for Space Vehicles. Aerospace Eng.,
    vol. 19, no. 12, Dec. 1960, pp. 20-23; 55-78.

TABLE I. - FIRING SCHEDULE

[356-T51 cast aluminum; columbium - 1 percent zirconium.]

Test variables	Test conditions	Target
Temperature	Room temperature, 400°, 600°, 700°, and 750° F	Aluminum armor cast on HS-25 liner
Impact angle - tube axis displaced	0°, 30°, 60°, and 75° to 80° at room temperature and 700° F	
Liner thickness	0, 0.020, 0.035, and 0.044 inch at 700° F	
Tube diameter	0.125, 0.46, a1.0, a2.5 inch, and ∞ at 700° F	0.446-inch-thick aluminum .320-inch-thick columbium
Material properties	Aluminum against equivalent mass of columbium Aluminum against equivalent protection of columbium 0.125- and 0.460-inch tube inside diameter at 700° F	0.446-inch-thick aluminum .202-inch-thick columbium .320-inch-thick columbium

aAluminum only.

TABLE II. - DETAILS OF FIRINGS

Target	Liner material	Liner inside diameter, in.	Liner thickness, t_l, in.	Armor material	Armor inside diameter, in.	Armor thickness, t_a, in.	Target temperature, °F	Target hardness at room temperature (R.T.), BHN	Projectile diameter, in.	Projectile mass, g	Projectile velocity, ft/sec	Impact angle, λ, deg	Crater diameter, in. Minimum	Crater diameter, in. Maximum	Crater depth, P, in.	Inside diameter below dimple, in.	Dimple height, h, in.	Ratio of crater depth to armor thickness, P/t_a	Young's modulus, Y_t, psi	Damage code	Crater depth corrected to 25,000 ft/sec, P*, in.
1	HS-25	0.460	0.020	Al	0.500	0.400	400	36	3/32	0.0160	25,500	5	0.45	0.52	0.299	0.34	0.12	0.747	9.4×10⁶	--	0.295
5	→	→	→	→	→		700	37	3/32	.0161	25,300	68	.35	.42	.168	.46	....	.420	6.8	--	.167
5							732	37	3/32	.0161	23,790	8	.50	.56	.306	.37	.09	.765	6.6	--	.316
6							R.T.	53	1/8	.0413	24,050	16	.52	.54	----	Perforated	Perforated	---	10.9	1e	Perforated
7							700	57	3/32	.0160	24,600	68	.31	.36	.127	.46	.12	.318	6.8	1b	.128
9							R.T.	36	1/8	.0160	24,300	15	.50	.58	.315	.34	.12	.787	↓	1e	.320
10								36	1/8	.0412	23,500	41	.63	.73	.476	.23	.23	1.19		1c	.496
12								37	3/32	.0413	22,700	0	.64	.78	----	Perforated	Perforated	---	10.9	1e	Perforated
15								36	1/8	.0160	24,350	0	.42	.47	.544	.26	.20	1.36		1c	.544
16						.350		51	1/8	.0414	24,000	10	.53	.50	.315	.33	.13	.786		1c	.323
26								36	3/32	.0160	23,950	33	.39	.45	.322	.37	.09	.920		--	.351
27	↓	↓	↓	↓	↓	.300	↓	38	3/32	.0160	25,300	32	.41	.47	.281	.34	.12	.937	10.9	--	.279
31	----	----	----	Cb	.460	0.200	700	121	3/32	0.0160	26,150	40	0.28	0.38	0.150	---	---	0.750	15.8×10⁶	2c	0.146
32	----	----	----	→	.460	.200	↓	125	→	→	25,150	12	.31	.33	.225	Perforated	Perforated	.941	↓	2d	Perforated
34	----	----	----	Al	.125	.239		134			25,400	10	.30	.33	1.134	.06	0.065	.420	↓	--	.235
37	----	----	----	Al	∞	.320		134			24,550	--	.30	.30	.290	---	---	.624	6.8	2c	.136
38	----	----	----		.420	.465		36			25,350	27	.50	.56	----	Perforated	Perforated	---	6.8	2c	.288
39	----	----	----	Cb	∞	.446		35			24,650	--	.48	.48	.135	Perforated	Perforated	.413	15.8	2d	Perforated
40	----	----	----	Cb	.460	.320		135			24,950	5	.30	.31	.109	.39	.05	.341	15.8	--	.136
41	----	----	----	Cb	.125	.320	↓	135			24,700	13	.28	.28	.351	.11	.015	.787	15.8	--	.110
45	----	----	----	Al	2.50	.446	500	36	→	→	25,400	0	.48	.50		---	---		8.8	2c	.348
53	HS-25	0.460	0.020	Al	0.500	0.400	R.T.	37	3/32	0.0160	24,750	70	0.36	0.36	0.158	0.46	---	0.395	10.9×10⁶	--	0.159
54	→	.402	.020	→		.400	R.T.	→	→	.0159	25,200	27	.50	.55	.252	.37	0.09	.630	10.9	--	.251
62		.460	.049			.343	700			.0157	23,000	65	.40	.43	.184	---	---	---	6.8	--	.195
64		.460	.020			.400	700			.0160	24,500	20	.51	.57	.386	.35	.11	.965	6.8	--	.394
66		.460	.020			↓	700			.0160	24,250	26	.53	.59	.314	.31	.15	.784	6.8	--	.320
69		.460	.020			.371	400			.0156	25,000	15	.50	.51	.306	.37	.09	.765	9.4	--	.306
71		.430	.049			.343	700			.0151	24,400	0	.44	.55	.319	.36	.07	.860	6.8	1c	.323
75		.403	.035			.446	↓			.0177	25,100	0	.52	.60	.372	.33	.072	1.08		1c	.372
79		----	----		.460	.446				.0152	24,700	0	.45	.53	.289	.36	.10	.647		--	.291
83		----	----		.125		56	20		.0148	24,600	20	.41	.46	.212	.10	.025	.476		--	.226
84		----	----		∞	1.20	R.T.	57		.0151	25,000	0	.40	.40	.241	---	---	----	10.9	2a	.241
85	↓	----	----	↓	∞	.96	R.T.	36	↓	.0176	24,700	0	.42	.42	.253	---	---	----	10.9	2a	.252

17

TABLE III. – COMPARISON OF MATERIALS CONSTANT FOR ALUMINUM AND COLUMBIUM TARGETS

(a) Aluminum (356-T51)

Target	Experimental P/d_p	Calculated $\left(\frac{V\cos\lambda}{c_t}\right)^{2/3}\left(\frac{\rho_p}{\rho_t}\right)^{\varphi}\left(\frac{P_t}{P_\infty}\right)$	Calculated γ	Calculated $(E/B\cos^2\lambda)^{1/3}$	Calculated K
1	3.19	1.36	2.34	....	....
3	1.79	.764	2.35	0.341×10^3	1.23×10^{-3}
5	3.26	1.425	2.29	$.589\times10^3$	1.37×10^{-3}
7	1.35	.762	1.78	$.326\times10^3$	1.00×10^{-3}
9	3.36	1.447	2.32	$.634\times10^3$	1.25×10^{-3}
27	3.00	1.16	2.59	$.450\times10^3$	1.57×10^{-3}
38	3.09	1.39	2.22	$.585\times10^3$	1.24×10^{-3}
53	1.68	.624	2.70	$.256\times10^3$	1.57×10^{-3}
54	2.69	1.19	2.26	$.494\times10^3$	1.29×10^{-3}
66	3.35	1.35	2.47	$.620\times10^3$	1.31×10^{-3}
69	3.26	1.34	2.44	....	....
71	3.90	1.64	2.32	$.641\times10^3$	1.28×10^{-3}
79	3.08	1.39	2.22	$.646\times10^3$	1.14×10^{-3}
83	3.26	1.80	1.83	$.584\times10^3$	1.42×10^{-3}
84	2.57	1.28	2.01	$.490\times10^3$	1.25×10^{-3}
85	2.70	1.28	2.12	$.517\times10^3$	1.25×10^{-3}
			Av. 2.27		Av. 1.30×10^{-3}

(b) Columbium – 1 percent zirconium

Target	Experimental P/d_p	Calculated $\left(\frac{V\cos\lambda}{c_t}\right)^{2/3}\left(\frac{\rho_p}{\rho_t}\right)^{\varphi}\left(\frac{P_t}{P_\infty}\right)$		Calculated γ		Calculated $(E/B\cos^2\lambda)^{2/3}$	Calculated K
		$\varphi = 1/2$	$\varphi = 2/3$	$\varphi = 1/2$	$\varphi = 2/3$		
31	1.60	0.819	0.685	1.96	2.34	0.290×10^3	1.27×10^{-3}
37	1.43	.935	.783	1.53	1.92	$.334\times10^3$	1.05×10^{-3}
40	1.94	.770	.645	1.23	1.42	$.344\times10^3$	1.00×10^{-3}
41	1.16	.935	.783	1.24	1.48	$.340\times10^3$	$.82\times10^{-3}$
				Av. 1.49	Av. 1.79		Av. 1.05×10^{-3}

Figure 1. - Fin and tube radiator.

Figure 2. - Impact crater in typical radiator section. Finned aluminum armor over HS-25 tube.
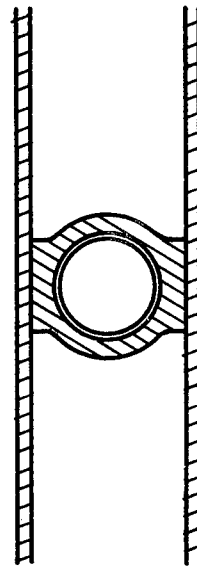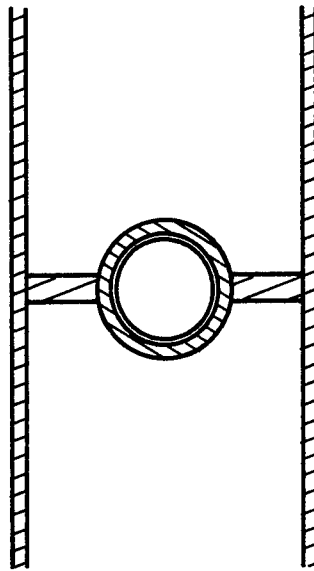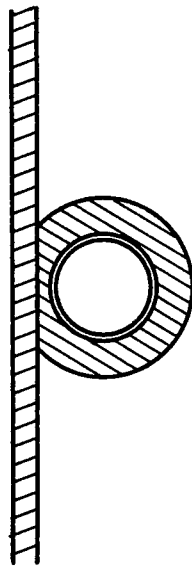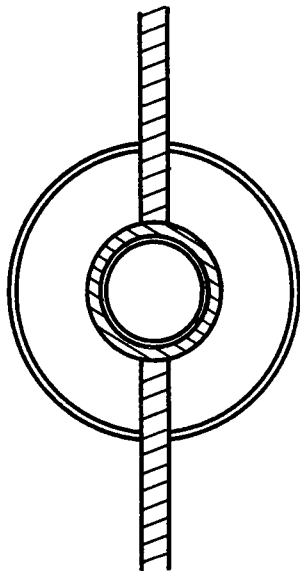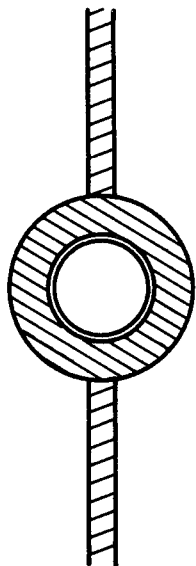
Figure 3. – Fin and tube geometries.
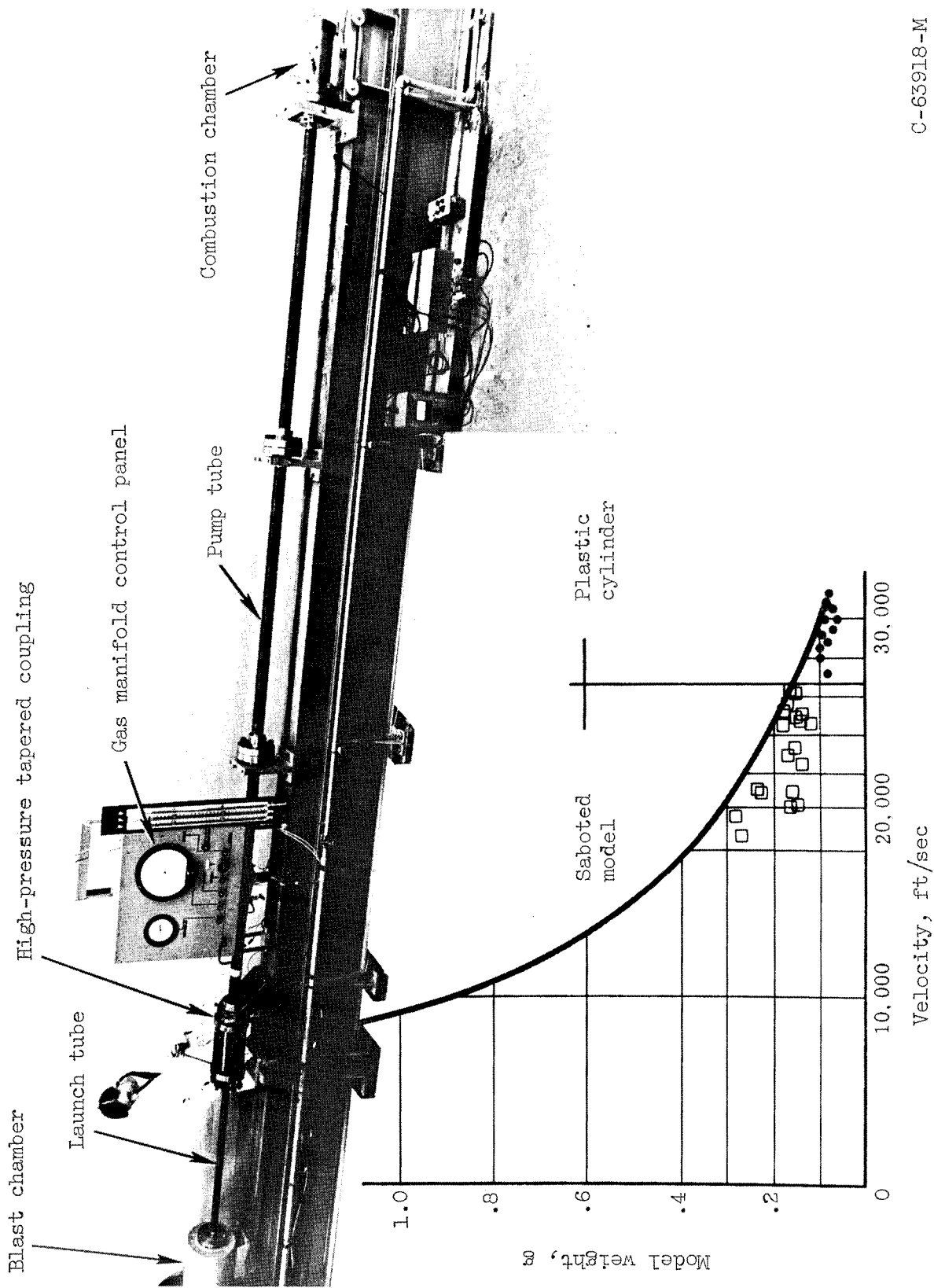
Figure 4. – Twenty-two caliber accelerated-reservoir light-gas gun.

C-63918-M
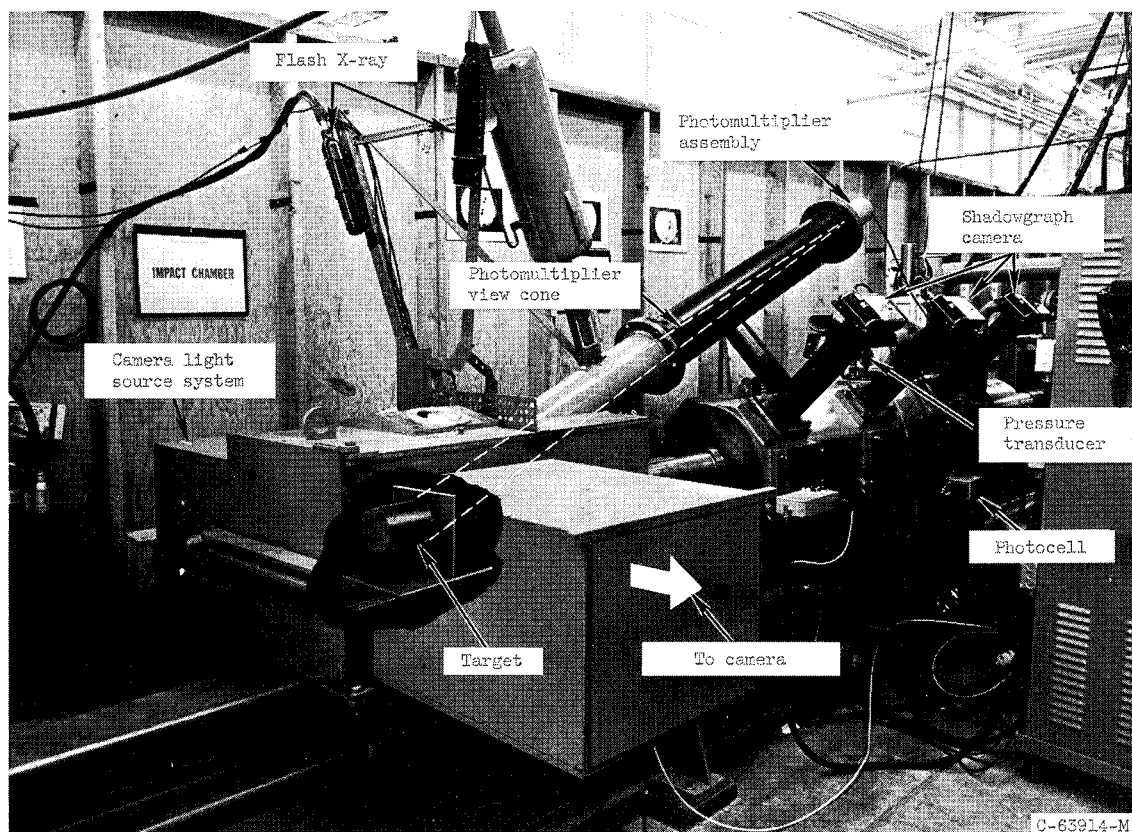
Figure 5. - Velocity and impact chambers.
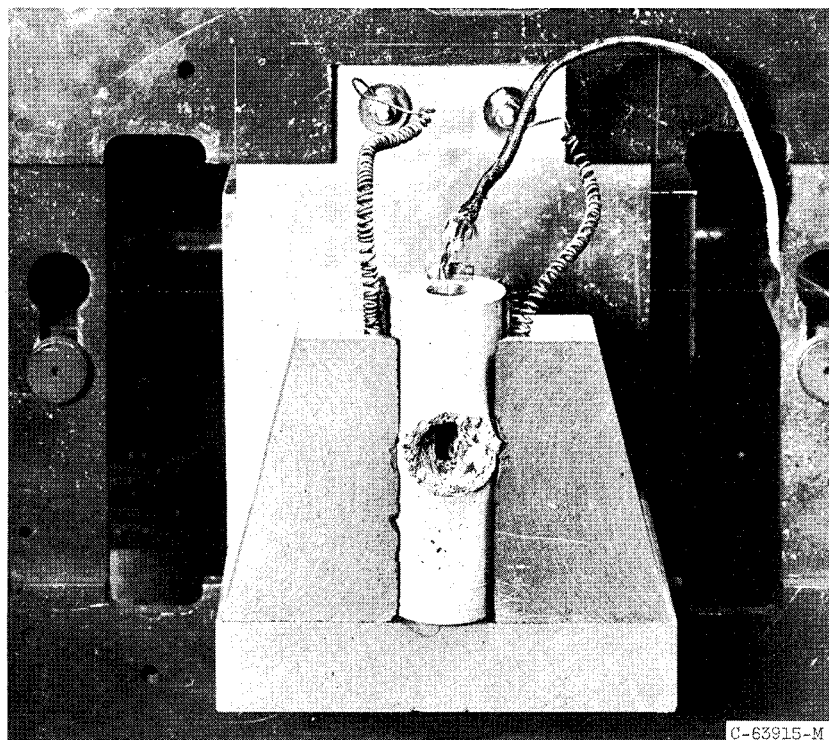
Figure 6. - Target holder with heater elements.

22
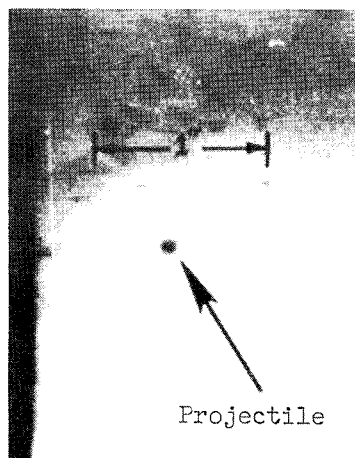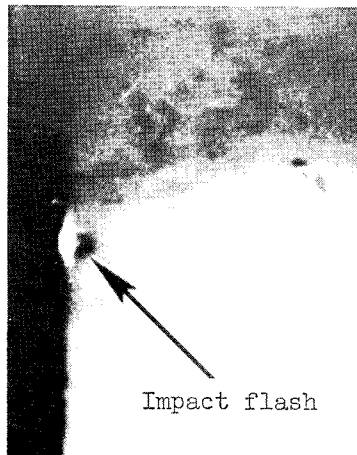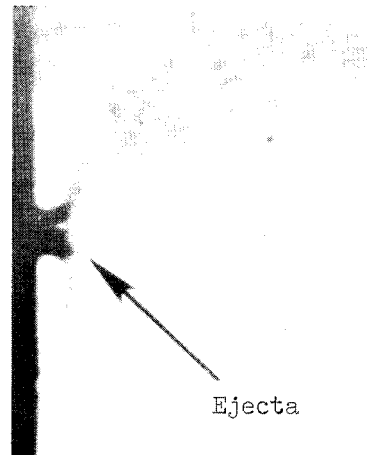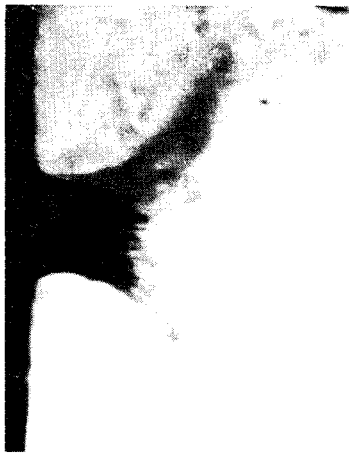
Projectile	Impact flash	Ejecta
-1.2 μsec	0 μsec	+1.2 μsec
+2.5 μsec	+6.2 μsec	+11.1 μsec
+21.0 μsec	+33.4 μsec	+44.5 μsec

C-63916-M

Figure 7. - Film sequence of a 1/8-inch glass sphere impacting a space radiator segment at 23,000 feet per second.

23
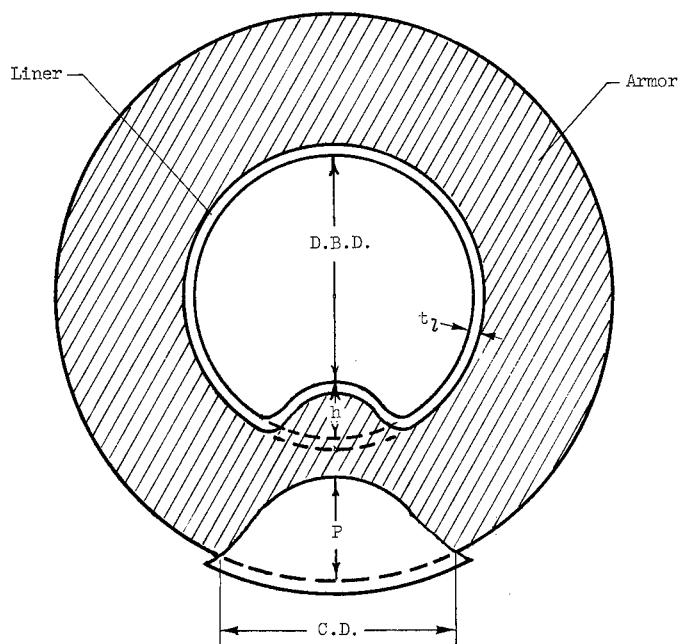
D.B.D. Inside diameter below dimple
  h   Height of dimple
  P   Crater depth
C.D.   Crater diameter
t_l Liner thickness

Figure 8. - Notation for target damage measurements.

C-63913-M
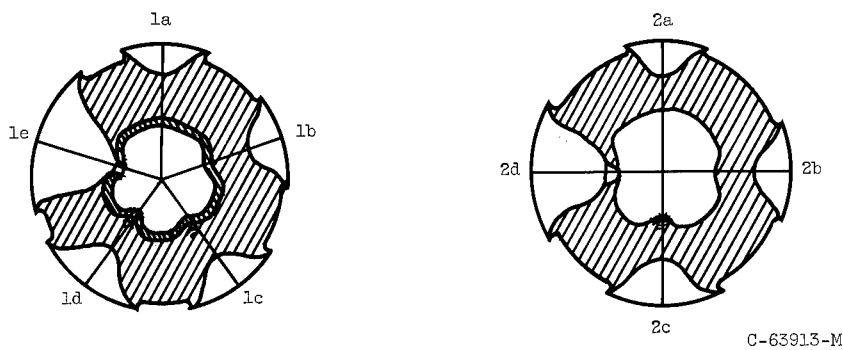
Type 1 - With liner

1a - C, N/D, N/S, N/P
1b - C, W/D, N/S, N/P
1c - C, W/D, A/S, N/P
1d - C, W/D, I/S, N/P
1e - C, W/P

Type 2 - Without liner

2a - C, N/D, N/S, N/P
2b - C, W/D, N/S, N/P
2c - C, W/D, I/S, N/P
2d - C, W/P

		Damage code number	
I.D.	Inside diameter	C	Crater
O.D.	Outside diameter	N/D	No dimple
t_l	Liner thickness	W/D	With dimple
t_A	Armor thickness	N/S	No spall
BHN	Brinell hardness number	I/S	Inner surface spall
R.T.	Room temperature	A/S	Armor internal spall
TAD	Target axis displaced	N/P	No perforation
TAR	Target axis rotated	W/P	With perforation
∞	Flat plate		

Figure 9. - Damage evaluation code for sectioned targets.
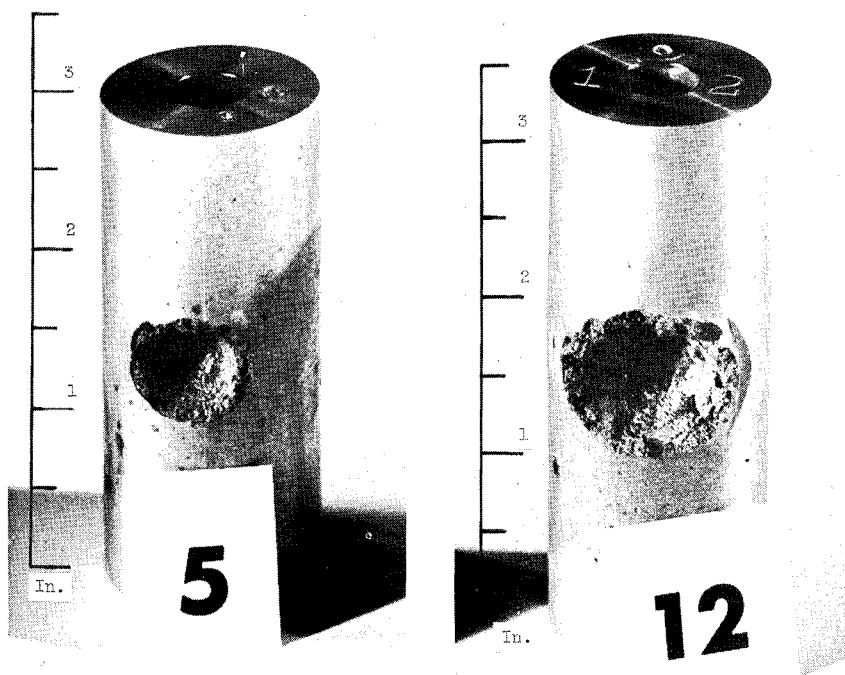
C-63912-M

(a) Glass sphere, 3/32 inch;
    no perforation; penetration,
    0.31 inch; liner dimpled.

(b) Glass sphere, 1/8 inch;
    perforated.

Figure 10. - Projectile size effects for aluminum with HS-25 liner targets.
Armor thickness, 0.400 inch; liner thickness, 0.020 inch; average velocity,
23,250 feet per second; temperature, 715° F.
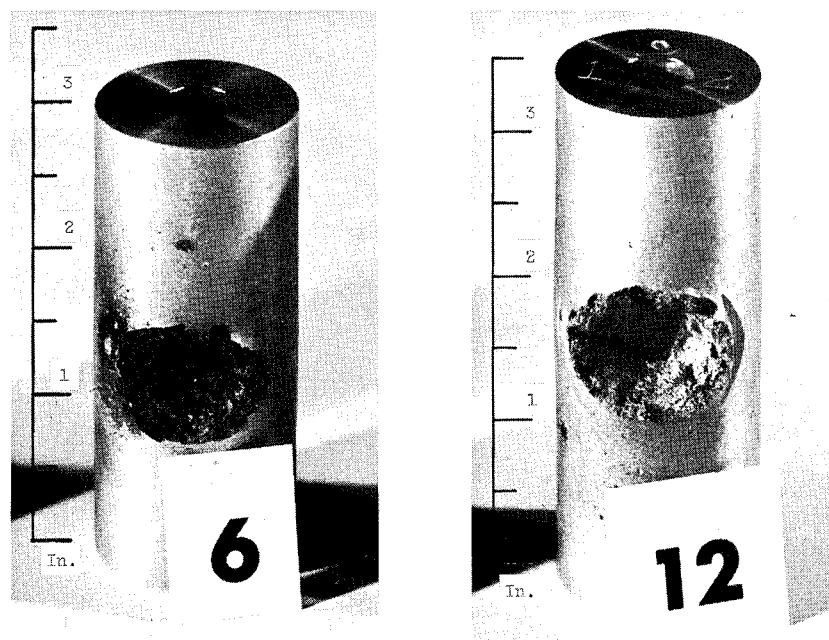
C-63917-M

(a) Room temperature; Brinell
    hardness number, 53.

(b) Temperature, 700° F; Brinell
    hardness number, 20.

Figure 11. - Target temperature effects for aluminum with HS-25 liner targets.
Armor thickness 0.400 inch; liner thickness, 0.020 inch; glass sphere, 1/8
inch; average velocity, 23,300 feet per second; specimens perforated.

25
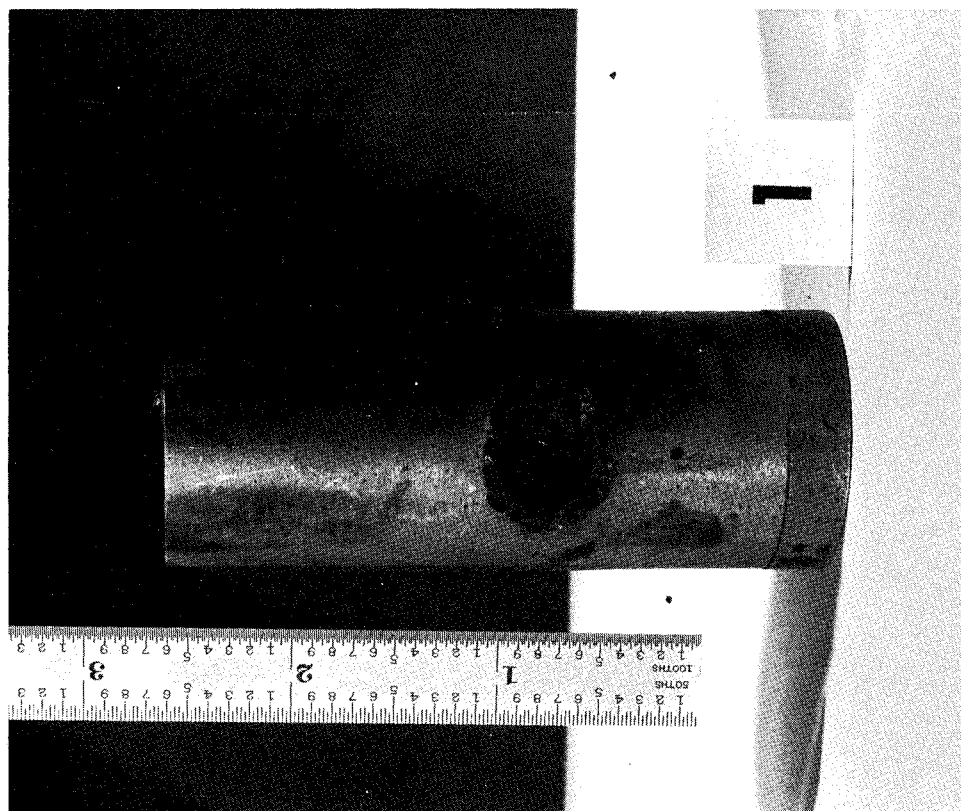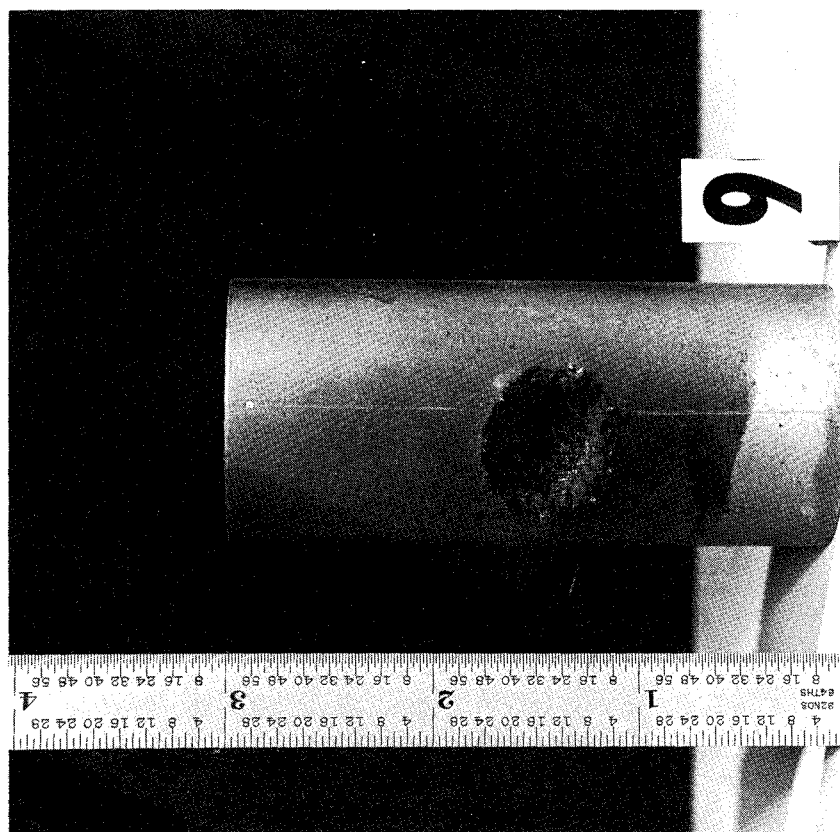
(a-1) Temperature, 400° F; Brinell hardness number, 25.　　　(a-2) Temperature, 700° F; Brinell hardness number, 20.

(a) View of crater surface.

Figure 12. - Target temperature effects for aluminum with HS-25 liner targets. Armor thickness, 0.400 inch; liner thickness, 0.020 inch; glass projectile, 3/32 inch; average velocity, 24,600 feet per second.

C-63920-M

26
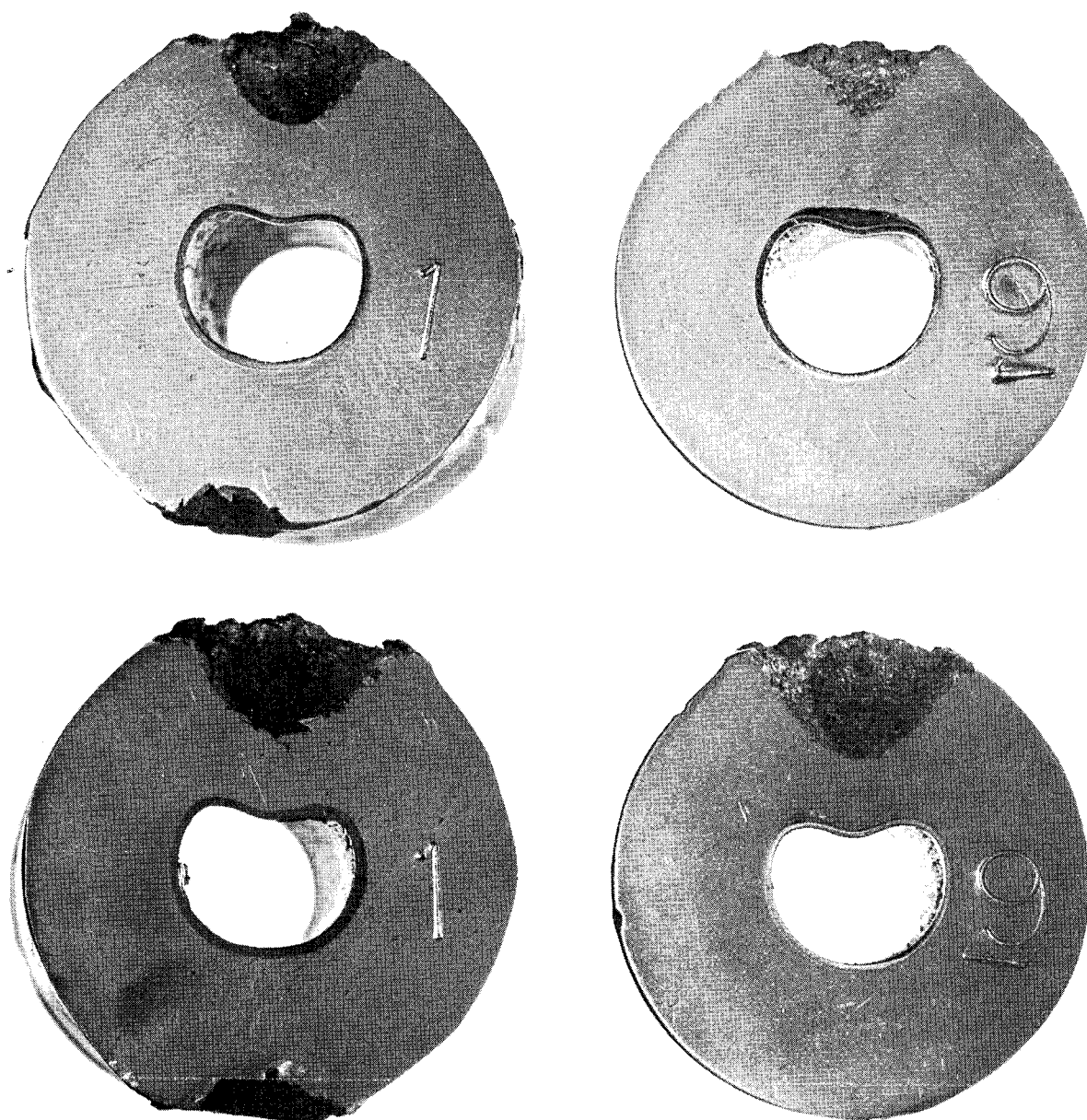
C-63921-M
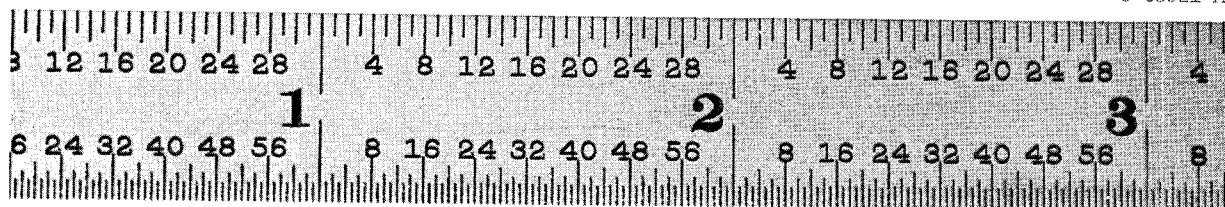
(b-1) Temperature, 400° F; Brinell hardness
  number, 25.

(b-2) Temperature, 700° F; Brinell hardness
  number, 20.

(b) Section view of crater at maximum depth.

Figure 12. - Concluded. Target temperature effects for aluminum with HS-25 liner targets.
  Armor thickness, 0.40 inch; liner thickness, 0.020 inch; glass projectile, 3/32 inch;
  average velocity, 24,600 feet per second.
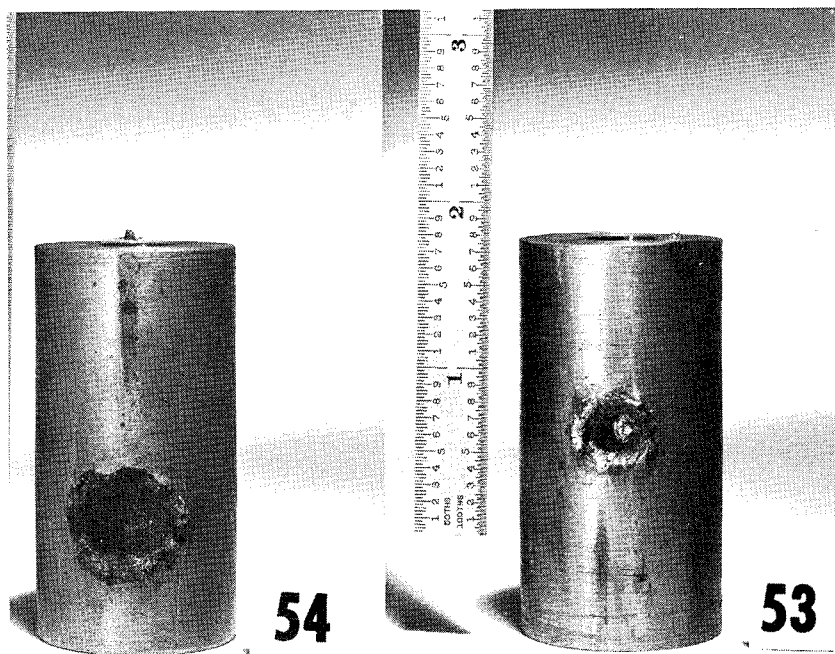
C-64100-M

(a) Impact angle, 27°; crater depth, 0.252 inch.

(b) Impact angle, 70°; crater depth, 0.151 inch.

Figure 13. - Impact angle effects for aluminum with HS-25 liner targets. Armor thickness, 0.400 inch; inside diameter of aluminum, 0.500 inch; glass sphere, 3/32 inch; average velocity, 24,900 feet per second; room temperature.
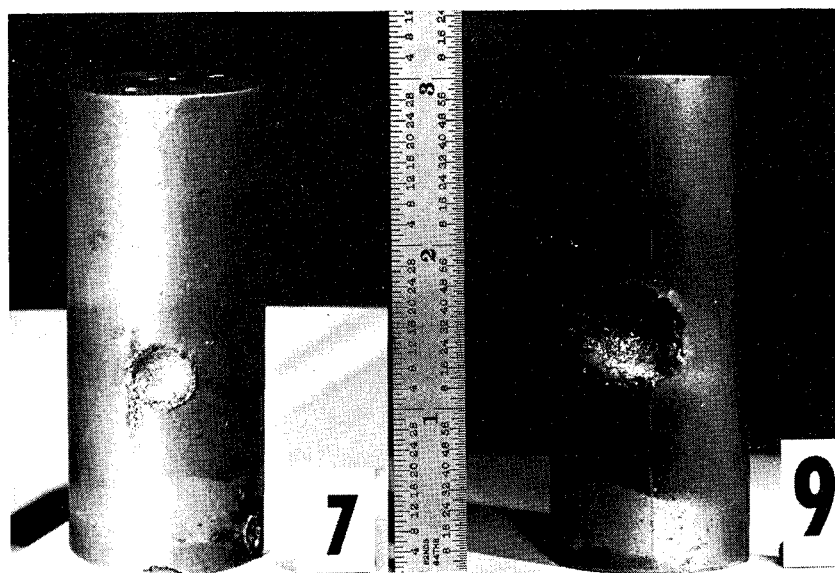
C-64409-M

(a) Penetration, 0.13 inch; impact angle, 68°.

(b) Penetration, 0.34 inch; impact angle, 15°.

Figure 14. - Impact angle effects for aluminum with HS-25 liner targets. Armor thickness, 0.400 inch; inside diameter of aluminum, 0.500 inch; glass sphere, 3/32 inch; average velocity, 24,450 feet per second; temperature, 700° F; no specimen perforation.
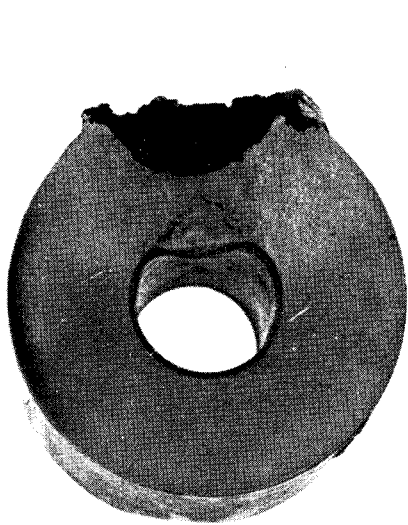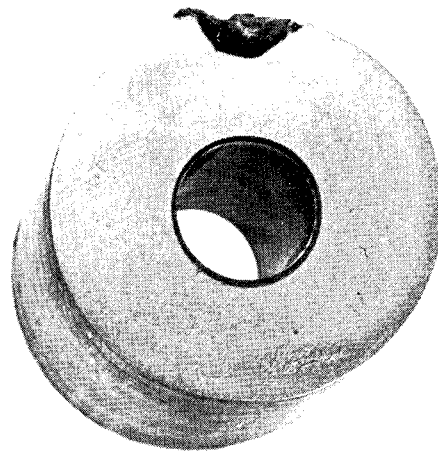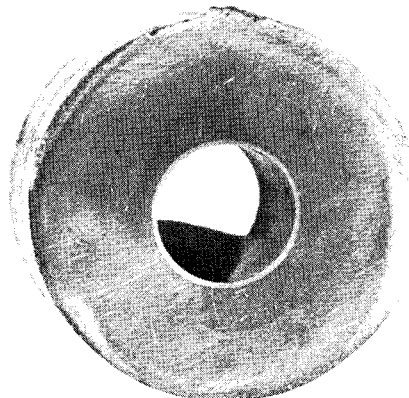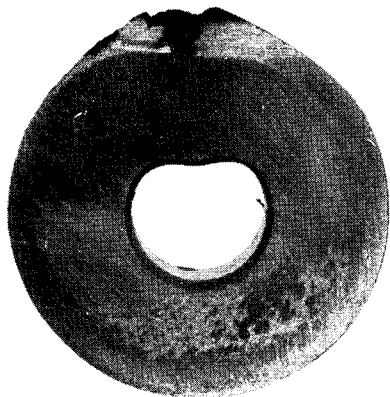
(a) Impact angle, 27°; crater depth, 0.252 inch.   (b) Impact angle, 70°; crater depth, 0.158 inch.

Figure 15. - Section view of crater. Impact angle effects for aluminum with HS-25;
armor thickness, 0.400 inch; inside diameter of aluminum, 0.500 inch; glass sphere,
3/32 inch; average velocity, 24,900 feet per second; room temperature.

29
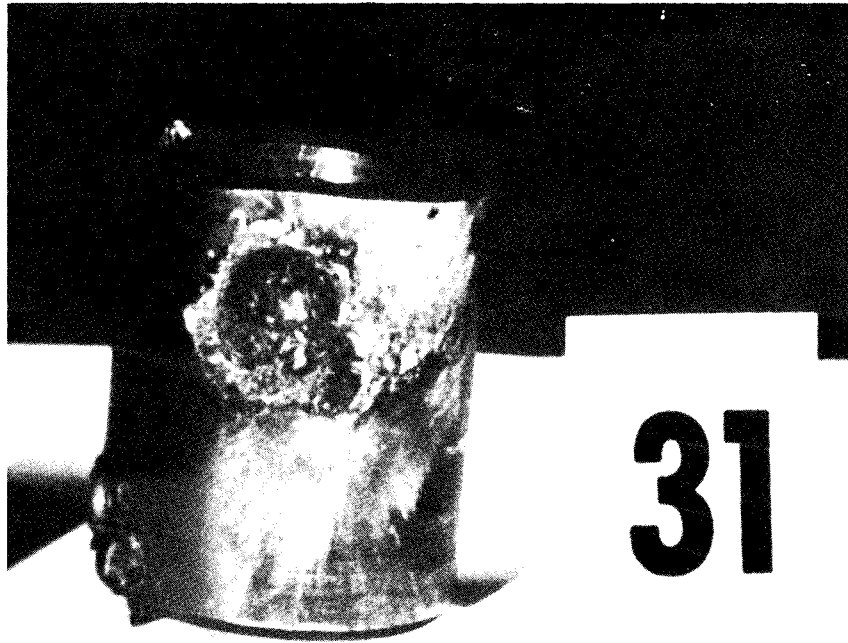
(a) Impact angle, 40°; no perforation; penetration, 0.150 inch.
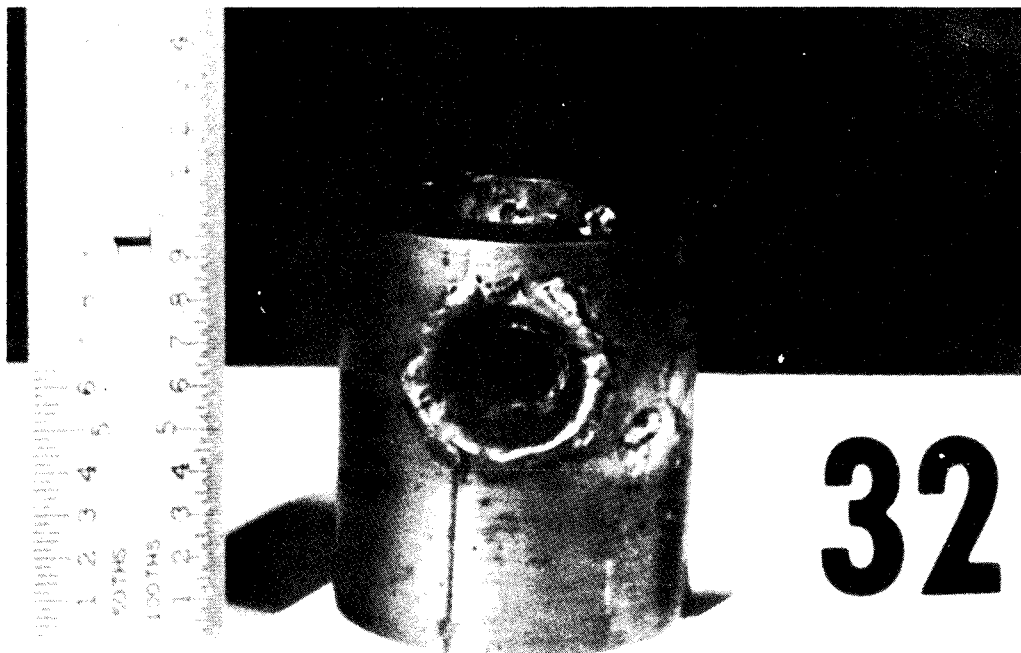
C-64104-M

(b) Impact angle, 12°; perforated.

Figure 16. - Impact angle effects. Armor thickness, 0.200 inch; inside diameter of columbium, 0.460 inch; no liner; glass sphere, 3/32 inch; average velocity, 25,650 feet per second; temperature, 700° F.
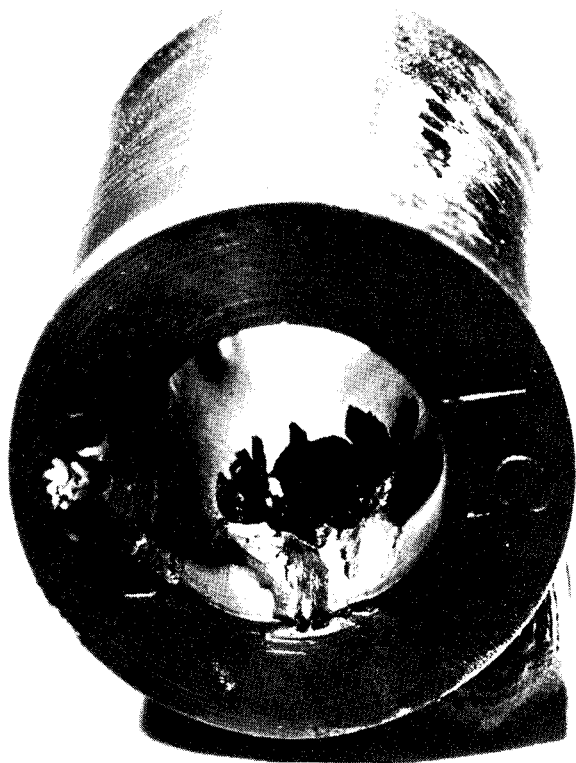
(a) Columbium wall thickness, 0.20 inch; internal
    spalling; glass sphere, 3/32 inch.

(b) Aluminum armor thickness, 0.40 inch; HS-25
    liner thickness, 0.02 inch; internal dimpling;
    glass sphere, 1/8 inch.

Figure 17. - Internal tube damage. Equal weight per unit length of tube; no perforation.
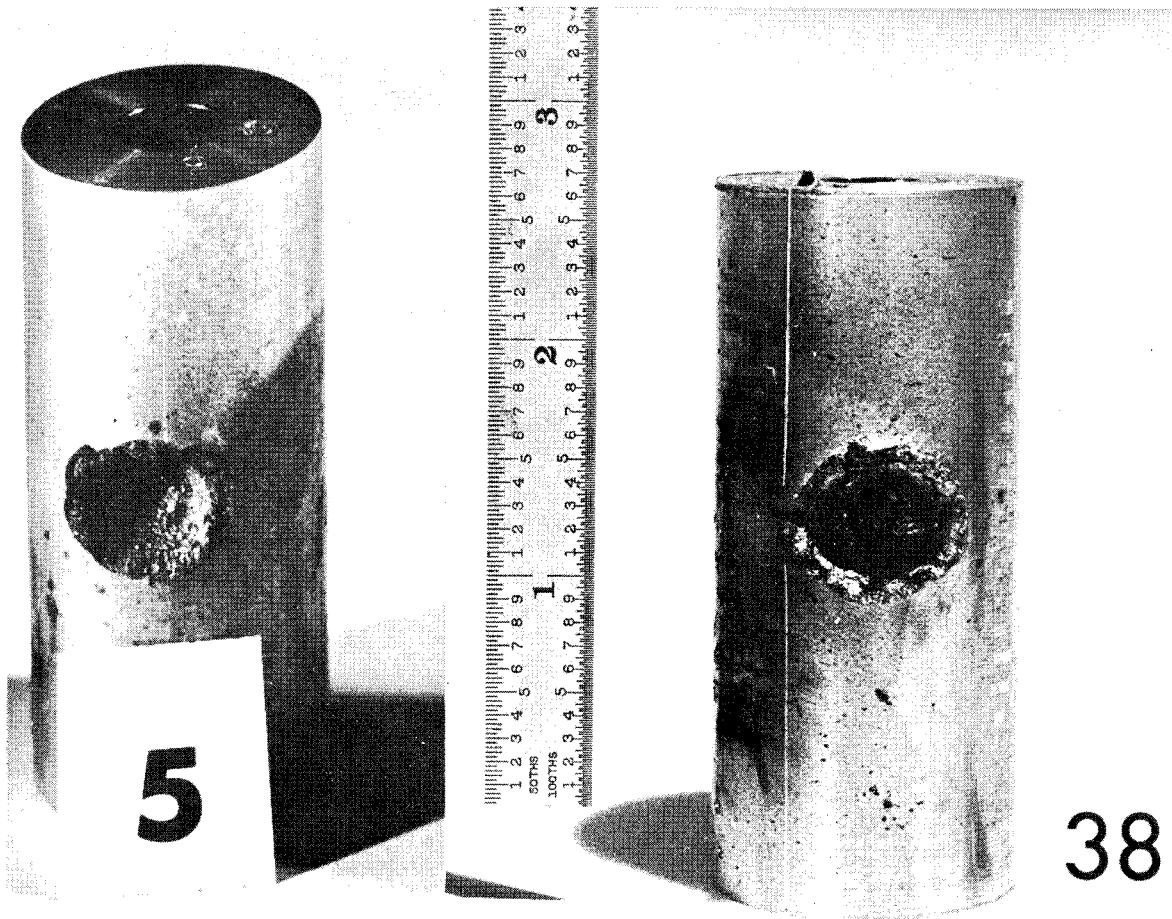
(a) Aluminum armor thickness, 0.40 inch; HS-25 liner thickness, 0.02 inch; no internal spalling; dimple on inside.

(b) Aluminum armor thickness, 0.47 inch; no liner; internal spalling.

C-64109-M

Figure 18. - Liner effects of aluminum targets. Equal weight per unit length of tube (approximately equal weight per unit length of radiator); no specimen perforation; glass sphere, 3/32 inch; average velocity, 24,650 feet per second; temperature, 715° F.
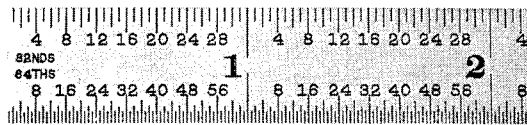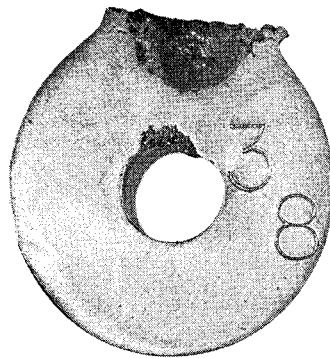
Figure 19. - Cross section of impact crater in unlined tube. Aluminum thickness, 0.47 inch; internal spalling; glass sphere, 3/32 inch; velocity, 25,350 feet per second; temperature, 700° F.
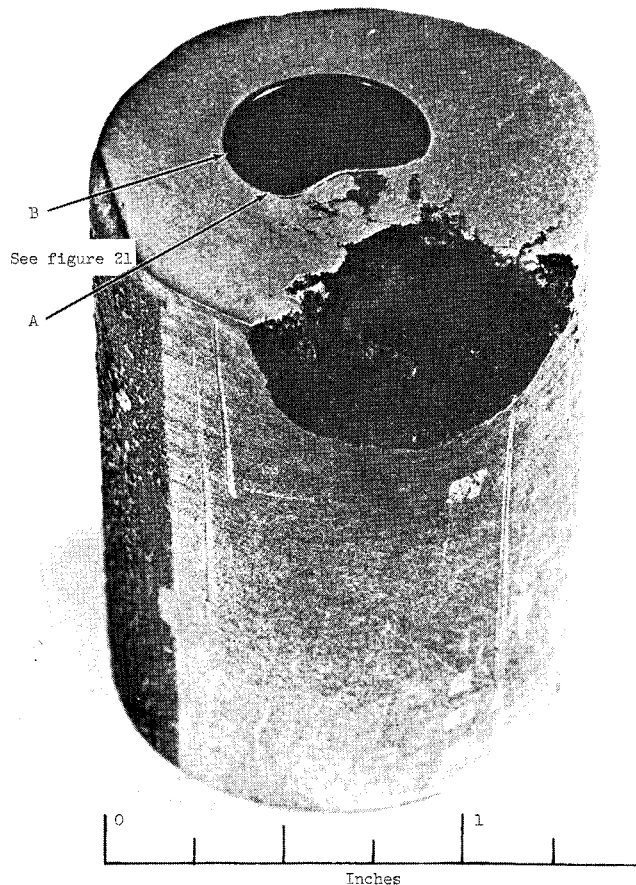
Figure 20. - Typical impact crater section. Aluminum armor with HS-25 liner.

Armor
(356 Al)

Liner
(HS-25)

(a) Section B. X300.

Delamination
of armor, bond,
and HS-25 tube

C-64108-M
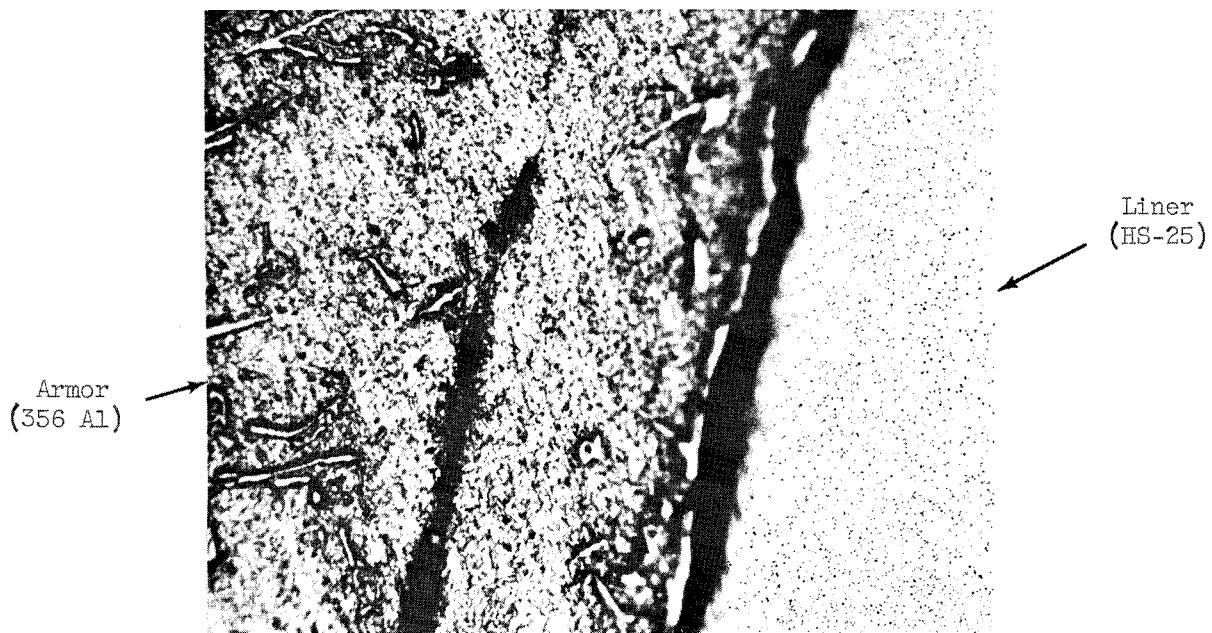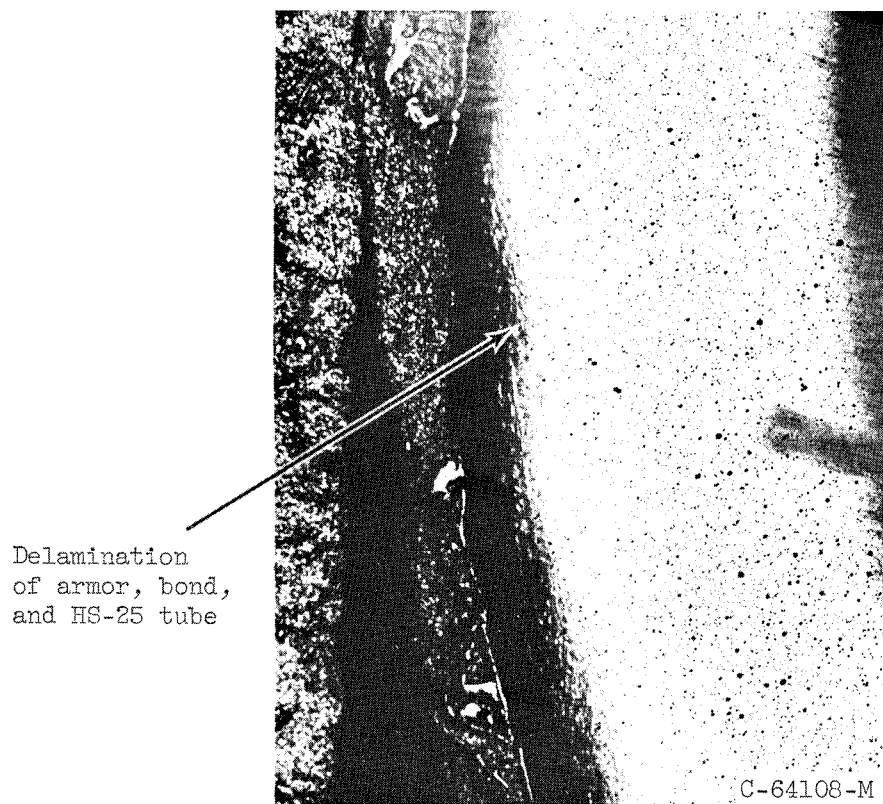
(b) Section A. X120.

Figure 21. - Armor-liner interface photomicrographs (see fig. 20).
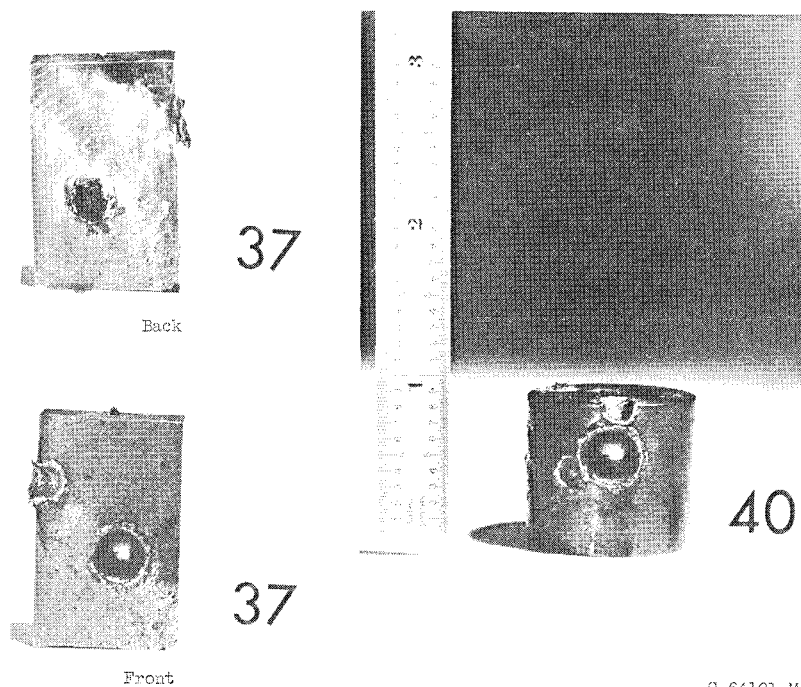
(a) Plate thickness, 0.320 inch; penetration, 0.134 inch; back spalling.

(b) Wall thickness, 0.320 inch; inside diameter, 0.460 inch; penetration, 0.135 inch; no internal spalling.

C-64101-M

Figure 22. - Target radius effects for columbium targets. Glass sphere, 3/32 inch; average velocity, 24,500 feet per second; temperature, 700° F.
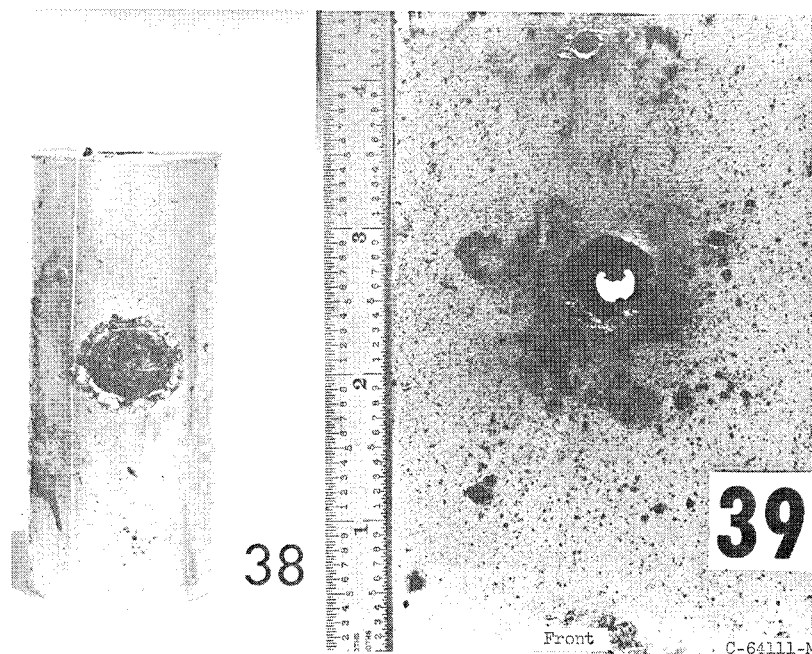
(a) Wall thickness, 0.465 inch; inside diameter, 0.420 inch; penetration, 0.290 inch; no perforation.

(b) Plate thickness, 0.446 inch; perforated.

C-64111-M

Figure 23. - Target radius effects for aluminum targets with no liner. Glass sphere, 3/32 inch; average velocity, 25,000 feet per second; temperature, 700° F.
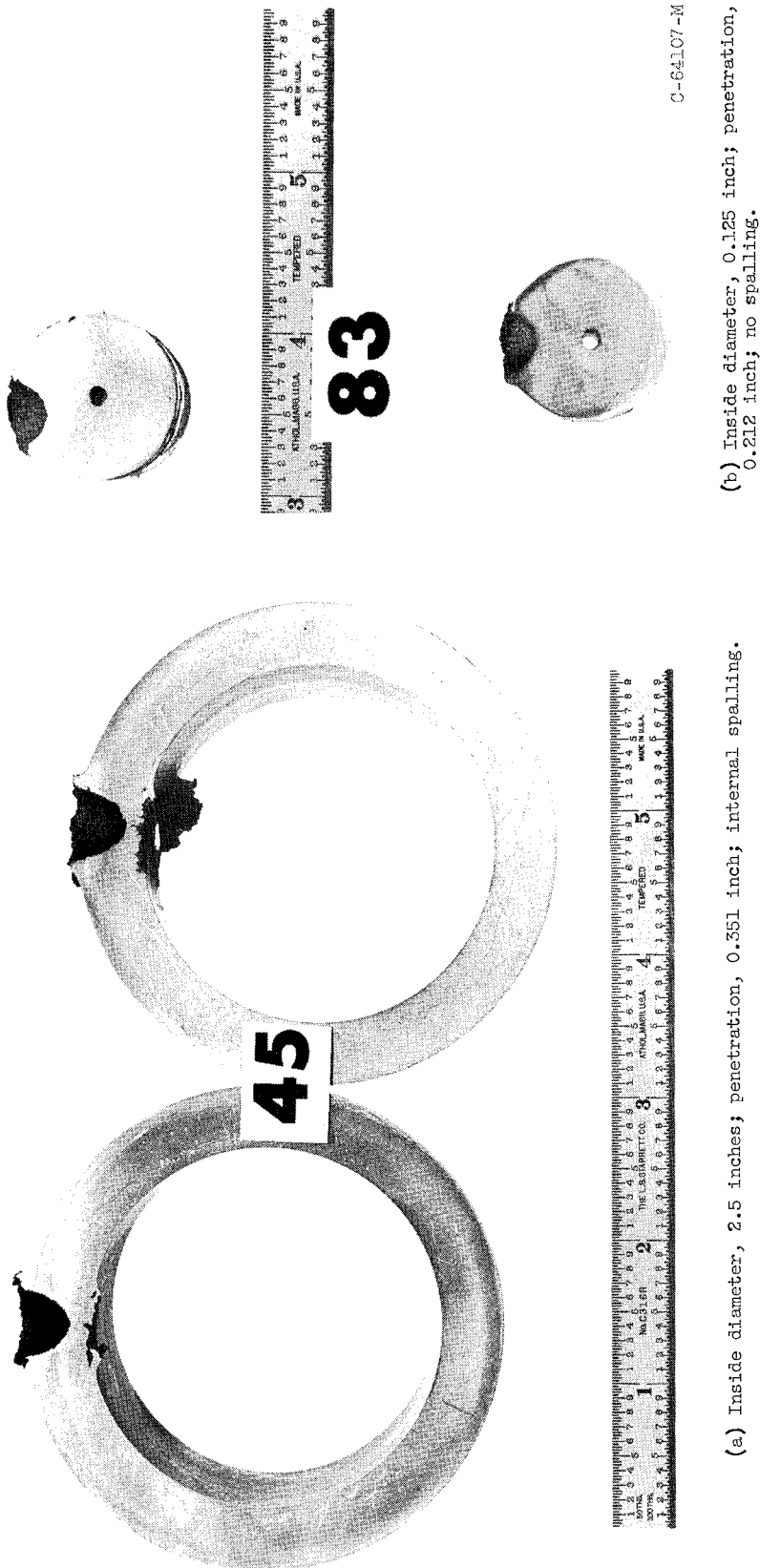
(a) Inside diameter, 2.5 inches; penetration, 0.351 inch; internal spalling.

(b) Inside diameter, 0.125 inch; penetration, 0.212 inch; no spalling.

C-64107-M

Figure 24. - Tube radius effects. Aluminum armor thickness, 0.446 inch; no liner; average velocity, 24,000 feet per second; temperature, 600° F.
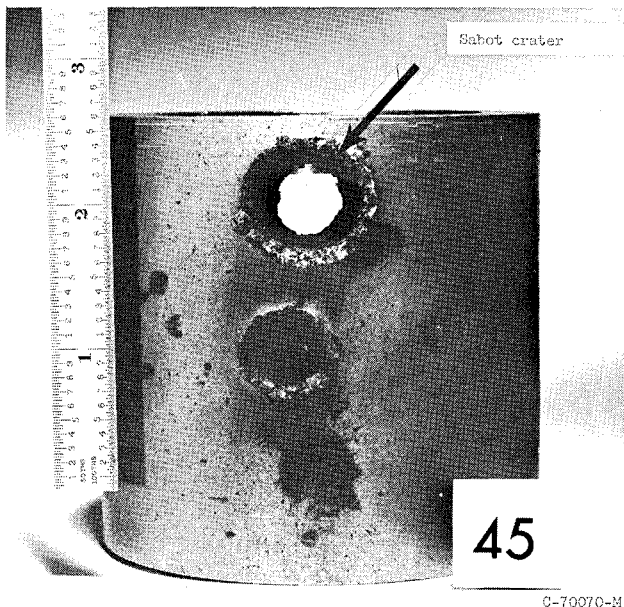
Figure 25. - Tube radius effects. Crater for 2.5-inch-inside-diameter target; aluminum armor thickness, 0.446 inch; no liner; glass sphere, 3/32 inch; velocity, 25,400 feet per second; temperature, 500° F.
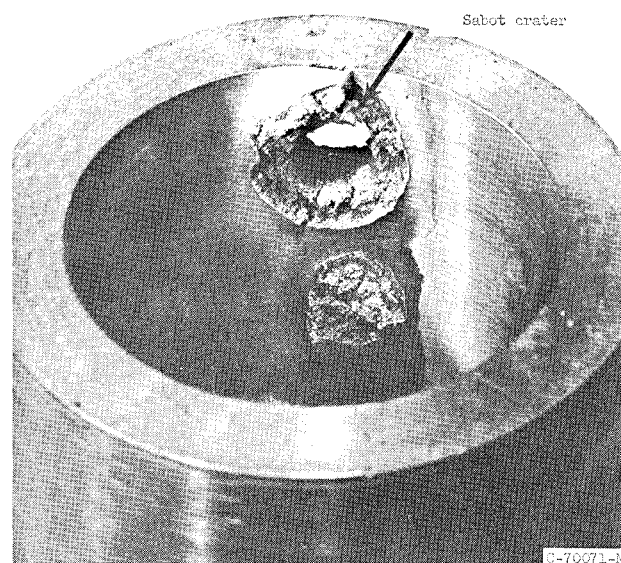

Figure 26. - Tube radius effects. Internal spalling for 2.5-inch-inside-diameter target; aluminum armor thickness, 0.446 inch; no liner; glass sphere, 3/32 inch; velocity, 25,400 feet per second; temperature, 500° F.
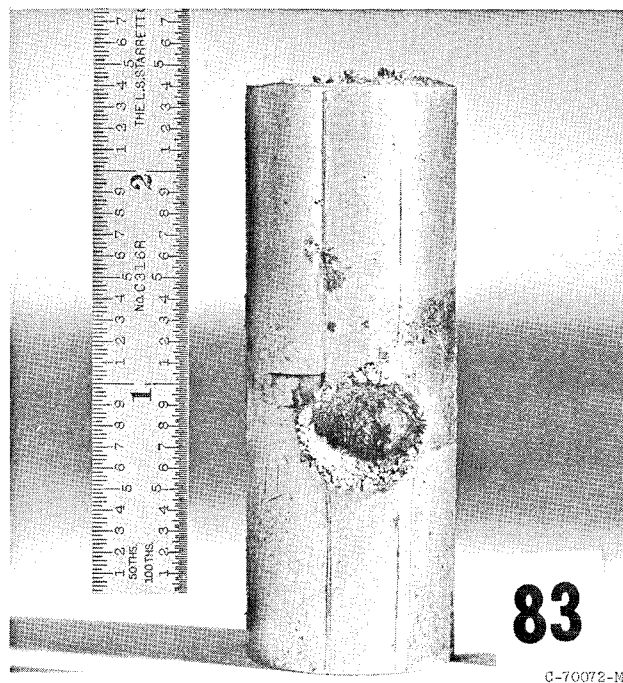
Figure 27. - Tube radius effects. Crater for 0.125-inch-inside-diameter target; aluminum armor thickness, 0.446 inch; no liner; glass sphere, 3/32 inch; velocity, 22,600 feet per second; temperature, 700° F.
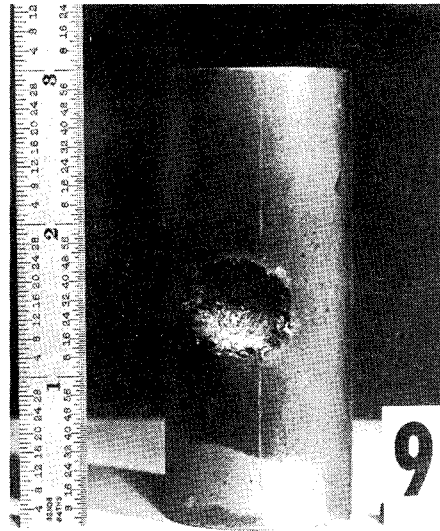
C-64102-M

(a) Columbium specimen; inside diameter, 0.460 inch; wall-thickness, 0.200 inch; perforated.

(b) Aluminum armor with HS-25 liner; inside diameter, 0.500 inch; wall thickness, 0.400 inch; penetration, 0.315 inch.

Figure 28. - Comparison of equal unit weight aluminum and columbium targets. Glass sphere, 3/32 inch; average velocity, 24,800 feet per second; temperature, 700° F.
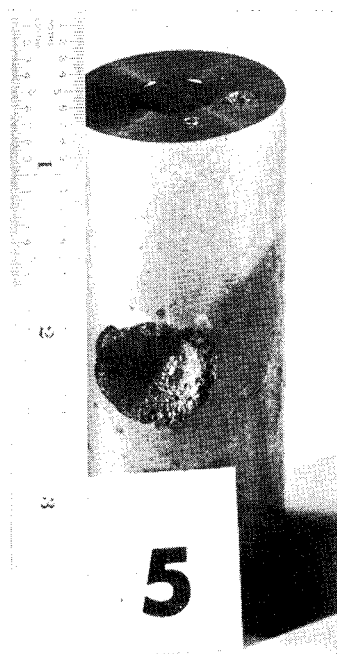
C-64105-M

(a) Aluminum armor with HS-25 liner. Wall thickness, 0.40 inch; liner thickness, 0.02 inch; penetration, 0.306 inch.

(b) Columbium specimen; wall thickness, 0.320 inch; penetration, 0.135 inch.

Figure 29. - Comparison of equal protection schemes (ref. 1). Constant inside diameter. Glass sphere, 3/32 inch; average velocity, 24,500 feet per second; temperature, 715° F.

38
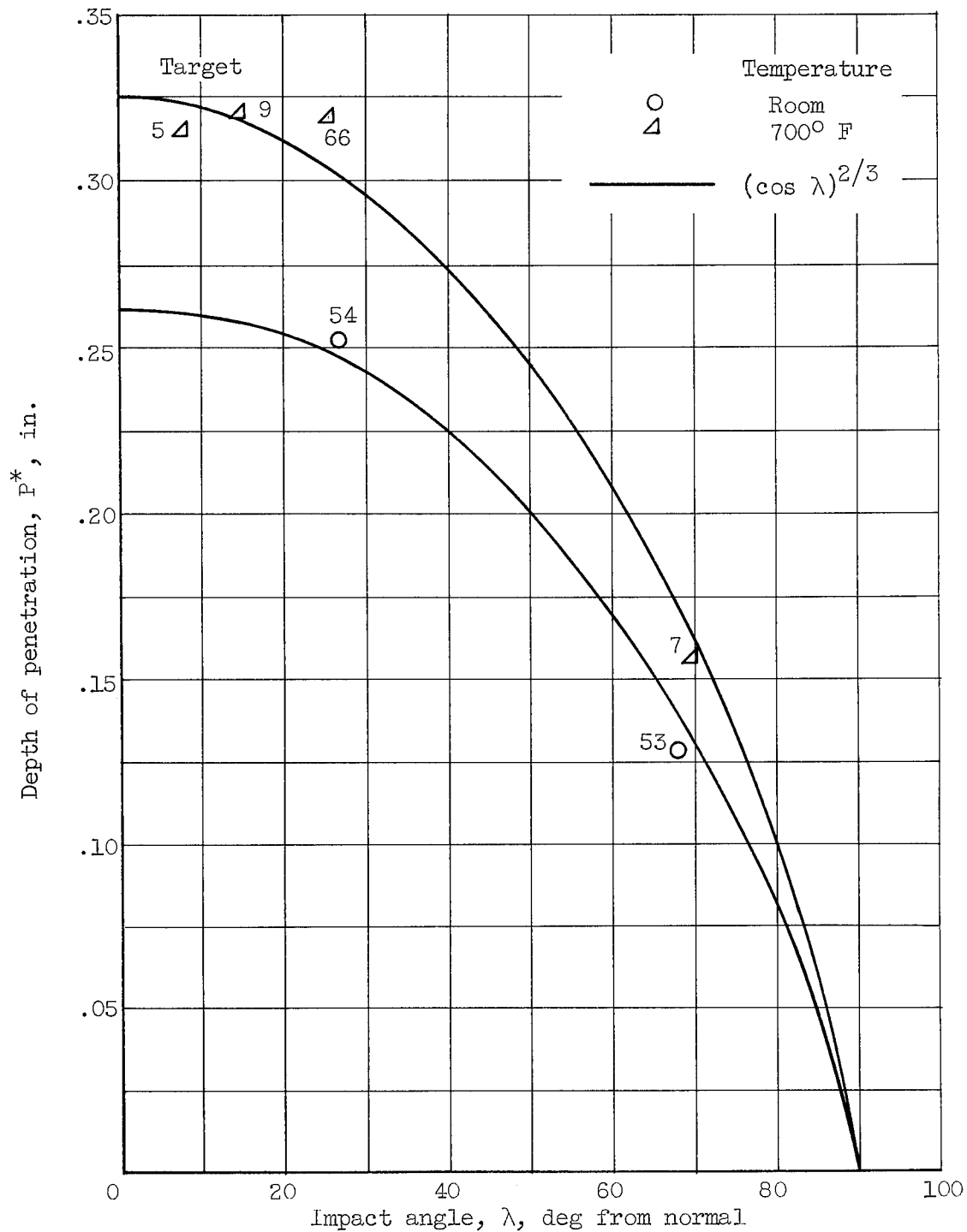
Figure 30. - Variation of penetration depth with impact angle.
Cast aluminum tubes; glass particle, 3/32 inch; velocity,
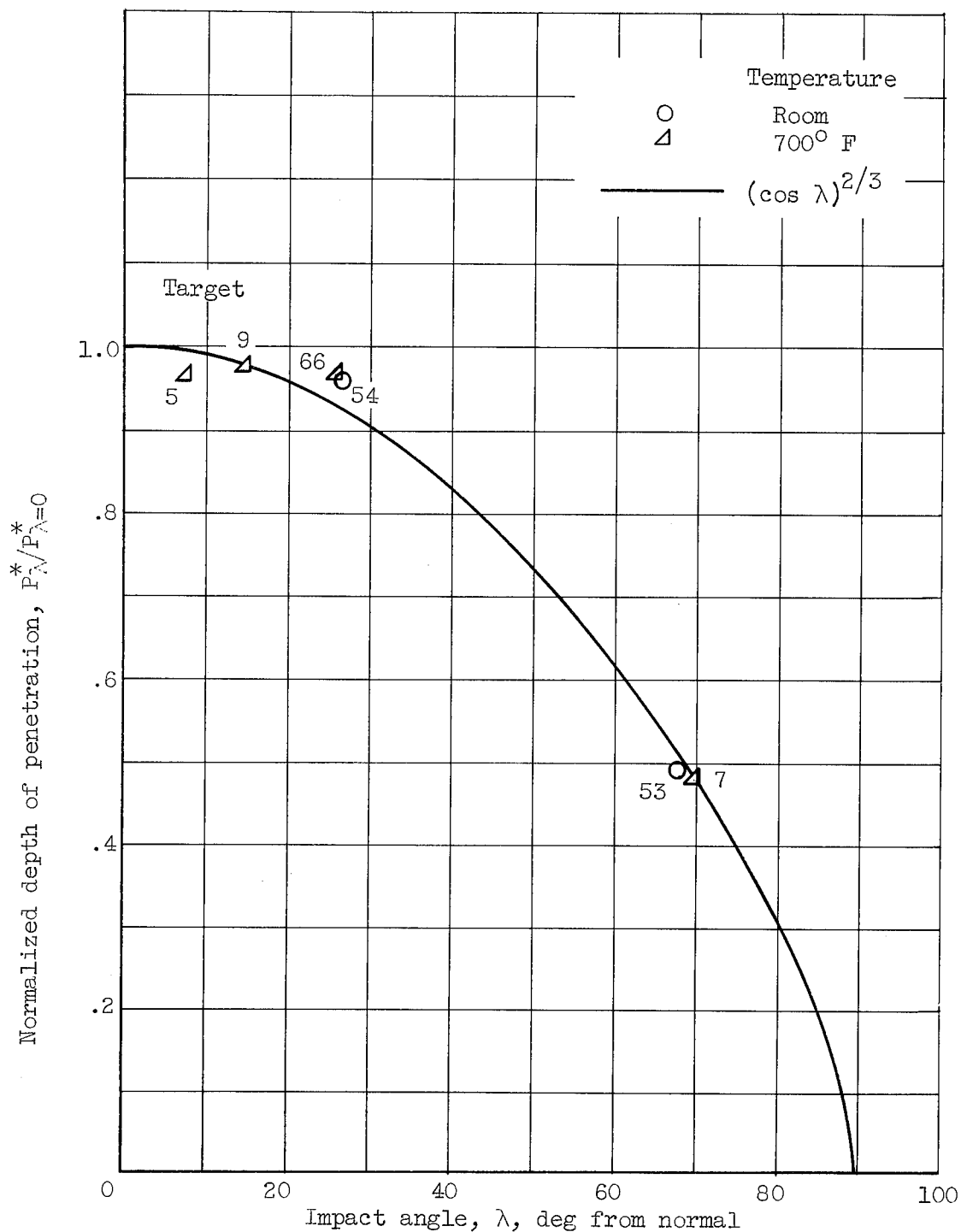25,000 feet per second.

Figure 31. - Normalized variation of depth of penetration with impact angle. Cast aluminum tubes; glass particle, 3/32 inch; velocity, 25,000 feet per second.
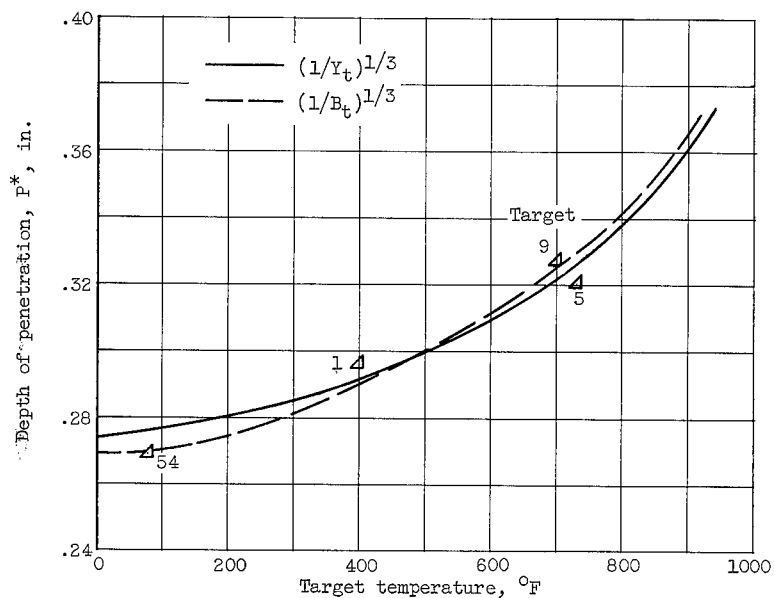
Figure 32. - Variation of depth of penetration with target
temperature. Cast aluminum tubes; normal impact; glass
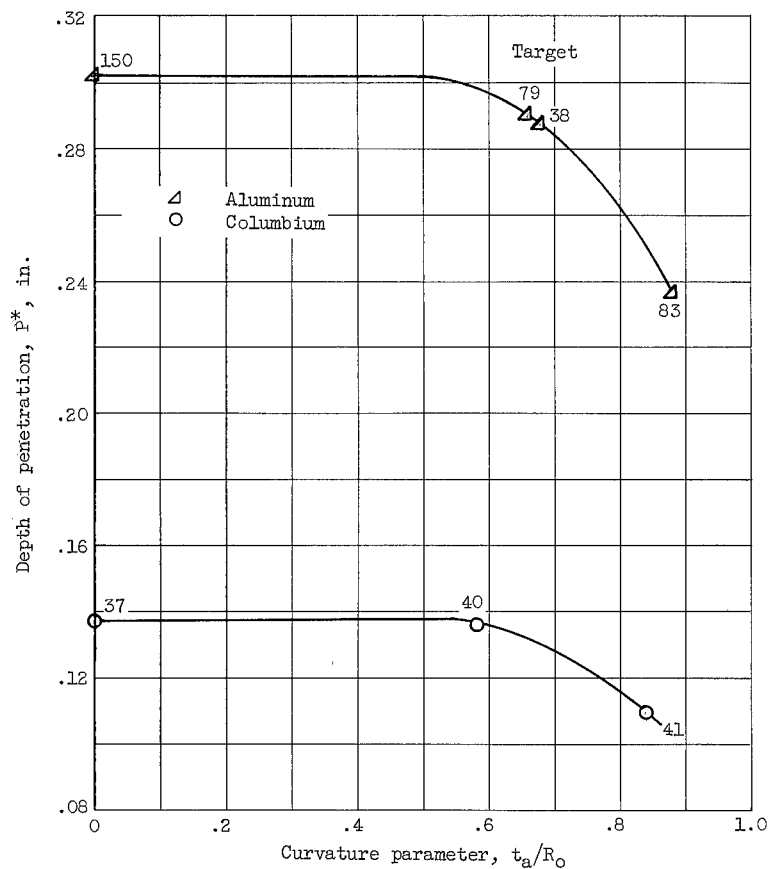particle, 3/32 inch; velocity, 25,000 feet per second.

Figure 33. - Variation of depth of penetration with tube ra-
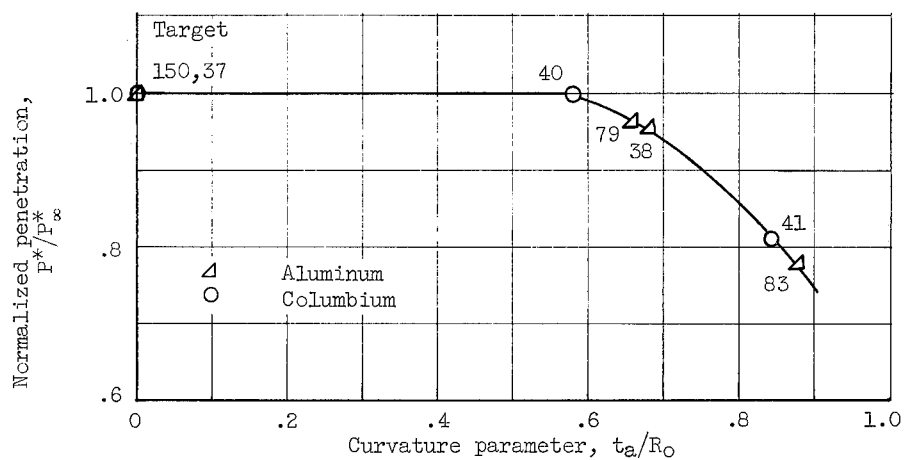dius. Temperature, 700° F; glass particle, 3/32 inch; ve-
locity, 25,000 feet per second.

41

Figure 34. - Variation of normalized penetration with tube
radius. Temperature, 700° F; glass particle, 3/32 inch;
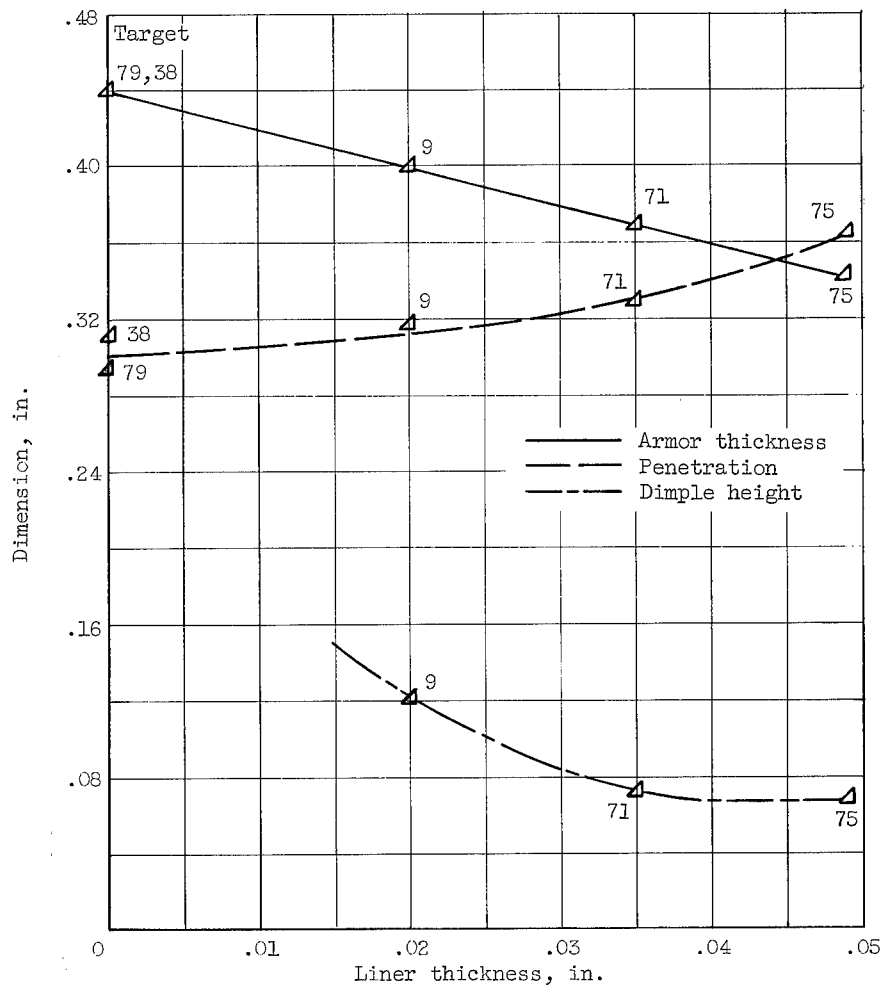velocity, 25,000 feet per second.

Figure 35. - Variation of depth of penetration and dimple
height with liner thickness. Cast aluminum on HS-25; equal
weight configurations.